

This is to certify that the
dissertation entitled

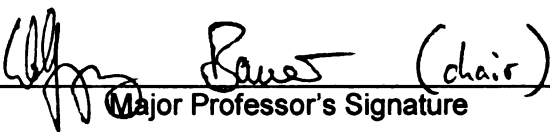
A HIGH-RESOLUTION SPECTROMETER
FOR RESONANT INELASTIC X-RAY SCATTERING

presented by

HASAN YAVAŞ

has been accepted towards fulfillment
of the requirements for the

Ph.D. degree in PHYSICS

 (chair)
Major Professor's Signature

12/14/07

Date

PLACE IN RETURN BOX to remove this checkout from your record.
TO AVOID FINES return on or before date due.
MAY BE RECALLED with earlier due date if requested.

DATE DUE	DATE DUE	DATE DUE

A HIGH-RESOLUTION SPECTROMETER FOR RESONANT INELASTIC
X-RAY SCATTERING

By

Hasan Yavaş

A DISSERTATION

Submitted to
Michigan State University
in partial fulfillment of the requirements
for the Degree of

DOCTOR OF PHILOSOPHY

Department of Physics

2007

ABSTRACT

A HIGH-RESOLUTION SPECTROMETER FOR RESONANT INELASTIC X-RAY SCATTERING

By

Hasan Yavaş

A better understanding of the dynamic behavior of correlated electron systems, such as transition metal compounds, may be realized by improving the energy resolution for resonant inelastic X-ray scattering (RIXS) technique. This dissertation proposes a new spectrometer with a relatively higher resolution, which is based on a back-reflecting sapphire crystal analyzer.

With this improved resolution, RIXS technique was used to measure the low-energy excitations in cupric oxide (CuO) as a function of incident photon energy. The measurements resulted in a remarkable change in the spectra depending on the energy of the incident X-ray beam.

To the memory of a good man,
my beloved friend
Mustafa Al-Haj Darwish

ACKNOWLEDGEMENTS

I consider myself fortunate for being able to follow my dreams and doing what I love to do. So far I have spent half my life learning physics, and doubtless it will be a lifelong pursuit that deserves constant questioning and exploration. As this journey cannot be pursued alone, it couldn't have started at all without the help of the people who were around me for the past six years. I owe gratitude to numerous people, without whom it would have been an impossible task.

I owe much to Dr. Ercan Alp for introducing me to the X-ray field, and encouraging and supporting me when needed. I learned the fundamentals of synchrotron research and how to become an experimentalist from him. I am also thankful to him for being a member of my advisory committee and his successful efforts in finding financial support for my classes at the University of Chicago and related travels. I feel fortunate to have Dr. Harald Sinn around me during the first few years of my research; I learned the principles of crystal X-ray analyzers from him. I would also like to acknowledge Dr. Wolfgang Sturhahn, Dr. Thomas Toellner, Dr. Yuri Shyv'dko, and Dr. Michael Lerche for helping me understand dynamical theory of diffraction and many stimulating discussions; Ahmet Alataş, Ayman Said, and all sector-3 crew for their guidance and support in the beamline and their friendship during the course of my research; Prof. Eldon Case for teaching me the silica layer bonding technique; Ruben Khachatryan and other Optics Fabrication group members for helping me fabricate the crystal analyzers and all the machinists at the central shops of the laboratory for making fabricating analyzers possible; Nadja Wizent from Dresden, Germany for making the CuO crystals on time and sending them to me. I am sure there are many others at the Advanced Photon Source that I forgot to mention here.

I would like to thank Prof. Simon Billinge for accepting me as a student and chairing the advisory committee. I am indebted for his continuous support and en-

couragement of my growth as an independent scientist. I would also like to thank Prof. Norman Birge, Prof. William Lynch and Prof. Bhanu Mahanti at the Michigan State University for accepting to be in my committee and their continuous guidance through many obstacles along the way.

I would like to acknowledge Prof. Zahid Hasan of Princeton University for helping me understand the RIXS experiments, inviting me to his beam-times and giving me confidence in my pursuit. I am also thankful to him for his financial support for over two years.

I would like to thank my friends at Michigan State University, especially Dr. Aous Abdo for the unending nights of problem-solving and pizza-eating sessions during the first year of our study and his continuing friendship. I feel lucky to have the following individuals around me: Murat Pırasacı being my roommate and a close friend for over five years; Eylül Wintermeyer; I am glad she exists and I thank her for her continuing kindness and support during a very stressful period of my life towards the end of my dissertation research, as well as the CDs she burnt for me. I also would like to thank the friends at the Turkish-American Cultural Alliance (TACA) and Turkish Consulate General in Chicago for helping me feel home thousands of miles away from home.

I cannot thank my parents enough for making me who I am and being my first mentors in life. Without their support and trust, this journey would have been an even harder challenge.

I finally acknowledge the support from DOE through grants DE-FG02-97ER45651 and DE-FG02-05ER46200. Use of the Advanced Photon Source was supported by the U. S. Department of Energy, Office of Science, Office of Basic Energy Sciences, under Contract No. DE-AC02-06CH11357.

Contents

List of Tables	vii
List of Figures	ix
1 Introduction	1
1.1 The Importance of Inelastic X-ray Scattering and a Brief History . . .	2
1.2 Scattering Cross Section	6
1.2.1 Resonant Inelastic X-ray Scattering with Momentum Resolution	13
1.3 Studies on Cupric Oxide (CuO)	15
2 Spectrometer Design	17
2.1 Perfect Crystals as Monochromators and Dynamical Theory	17
2.2 Instrumentation Related to Inelastic X-ray Scattering	23
2.2.1 Angular Acceptance	27
2.2.2 Geometrical Contributions and Demagnification	30
2.2.3 Energy Scanning	32
2.3 Analyzer Design	34
2.3.1 Crystal Selection	34
2.3.2 Cutting, Dicing, and Etching	35
2.3.3 Bonding Sapphire Wafers	40
2.3.4 Step by Step	41
3 Performance Assessment of the Spectrometer: Be Phonons	42
3.1 Characteristics of the Analyzer	43
3.1.1 Resolution Measurements	43
3.1.2 Energy Scanning and Calibration of the Instrument	45
3.2 Sample and the Sample Environment	49
3.3 Detector	51
3.4 Results	52
4 RIXS Study on Phonons in CuO	57
4.1 Background and Motivation	57
4.2 Experimental Details	59
4.3 Discussion	61
5 CONCLUSION	71
5.1 Future Outlook	72

A Instrument Parts	73
A.1 Engineering Drawings of the Heat Exchange Chamber	74
Bibliography	81

List of Tables

1.1	The high-resolution IXS spectrometers with <i>meV</i> -resolution available as user facilities	12
2.1	Potential use of sapphire analyzers for various transition metal K edges	34
2.2	Mohs Hardness Scale	38

List of Figures

1.1	The accessible range for different spectroscopic techniques. The horizontal axis is the momentum range, which is important to probe the spatial dispersion of the excitations to be investigated. The vertical axis is the frequency, which is the energy divided by \hbar	4
1.2	Inelastic scattering in the graph includes mainly the Compton scattering (big and ~ 200 eV-wide hump starting from ~ 9700 eV) and the Raman scattering (in this case, it is the Oxygen K-edge as the energy transfer is around 550 eV). Elastic scattering peak in this graph actually contains other inelastic scattering features but they are not visible due to low resolution (From ref. [1], reproduced with permission) . .	5
1.3	Top graph: the polarization (electric field) of the incoming wave is on the scattering plane. Bottom graph: the momentum transfer is perpendicular to the polarization of the incoming field (Figure reproduced from ref. [2]).	7
1.4	A general scattering geometry, where k is the wave vector of the incoming beam and k' is that of the scattered beam with a scattering angle of θ	10
1.5	Schematic representation of RIXS processes. Photon with frequency ω_{in}^0 excites a 1s electron to a 4p state. The core-hole potential <i>shakes-up</i> the system and causes excitations (it is an electron-hole pair in this case) in the valence states (for cuprates, it is the hybrid level of Cu-3d and O-2p). The excited electron fills the core-hole by emitting a photon with a frequency equal to the frequency of the incoming photon minus the expense of the excitation. Figure reproduced from ref. [3] with permission.	13
2.1	The inter-atomic spacing is d and the condition for Bragg diffraction is $n\lambda = 2d\sin\theta$. n is an integer, equal to 1 for the first harmonics and will be omitted during the subsequent discussion.	18
2.2	An asymmetric crystal with the asymmetry angle of η	20

2.3	A typical IXS spectrometer at a synchrotron. Here are the specific details for the test experiments at station 30 ID at the Advanced Photon Source: Undulator : 2-in-tandem, 3.0 cm period, each 2.4 m long, HMLM : High Heat Load Monochromator, C (1 1 1) double crystal diamond, IC : Ion Chamber to count the number of incident photons for normalization purposes, HRM : High Resolution Monochromator, Si (4 4 4) in nested geometry, Analyzer : Al ₂ O ₃ (0 4 14) diced, spherically bent crystal analyzer, Detector : Solid state diode detector . . .	24
2.4	The first and the fourth surfaces are made by cutting a channel from a single piece of crystal, the second and the third are another channel cut.	24
2.5	Rowland circle. A source on any point on the circle has a focal point on the same circle.	26
2.6	An illustration of a row of pixels. Individual flat and stress-free crystal pieces make up the spherical surface.	27
2.7	Bragg reflection is for plane waves (point source at infinitely large distance). For the case of spherical waves, the glancing angle for the incident beam at two different point on a crystal surface is not equal. This angular variation contributes to the energy bandwidth.	28
2.8	Graphical representation of Bragg equation. For the same $\Delta\theta$ the energy variations are shown at two different Bragg angles.	29
2.9	Intrinsic angular acceptance for a given Bragg reflection increases as the Bragg angle approaches to 90°.	29
2.10	A focusing mirror can be thought of as a concave mirror as the demagnification relations are identical.	31
2.11	Silicon and germanium share the same simple cubic diamond structure with lattice parameters 5.431 Å [4] and 5.658 Å [5], respectively. . . .	35
2.12	Sapphire has a hexagonal unit cell (R3c) with lattice parameters $a = b = 4.759$ Å and $c = 12.991$ Å [6].	36
2.13	Back-scattering parameters are calculated according to dynamical theory of diffraction at 300 K. Red lines indicate the K-edge energies of the transition metal oxides. Blue lines are the unique back-reflections with their height showing the reflectivity. Sapphire, clearly, has much more distinct back-reflecting planes compared to Si and Ge.	37
3.1	Overall instrumental resolution functions measured by two different scanning techniques. Open squares show the data taken by scanning the incident energy when the analyzer energy is kept constant. Open circles represent the data for the case when the incident energy is constant and analyzer temperature is scanned as a way of energy scanning.	44

3.2	The fit function (blue) is a pseudo-Voigt function, which is a linear combination of a Lorentzian and a Gaussian. The solid and dashed lines show the normalized Lorentzian and Gaussian component of the fit, respectively. Y-axis is in log scale to see the tails better.	45
3.3	Linear thermal expansion coefficient of sapphire for the direction parallel to c-axis (solid black) and for the direction perpendicular to c-axis (dashed red). At temperatures below 100 K, it approaches to zero and further cooling does not change the lattice parameters much. The inset has the portion accessible with the current instrumental limits.	46
3.4	On the top graph, every single peak corresponds to an individual energy scan that is performed by changing the incident energy. Incident energy can be calculated precisely as the goniometers used are connected to encoders with 10^{-5} ° precision, which gives an accuracy of $\sim 0.5 \mu\text{eV}$ in energy for the current setting. Since the energy scans are much faster than the energy change due to the temperature variation, the uncertainty involved here can be neglected. The blue (red) curve shows the angle of the outer (inner) pair of the monochromator crystals. In the zoomed view, both angles are scanned in the same direction. The only reason is to avoid the backlash of the scanning motors. This should not cause any confusion.	50
3.5	Detector from the side view. Spherically scattered beam (red) from the sample is focused (blue) on the detector chip after back-reflection from the analyzer. Detector housing material should be chosen so that the fluorescence radiation energy can be discriminated from the primary signal energy with detector's resolving power. Aluminum is a good choice for copper edge experiments.	52
3.6	Individual spectra measured at six different momentum transfer values defined by $\zeta \frac{2\pi}{c}$	55
3.7	Be phonon dispersion measured along the (0 0 ζ) direction, where momentum transfer vector is along the c-axis with magnitude equal to $\zeta \frac{2\pi}{c}$. Measurements are compared to published data by Alatas [7] (solid black circles) and Stedman [8] (dashed line).	56
4.1	Monoclinic structure of CuO. Oxygen atoms (small red) around copper atoms (big blue) form a ribbon-like bands along (1 1 0) and (1 -1 0).	58
4.2	The red (dashed) line shows the fluorescence spectrum across the copper K-edge absorption while the blue (solid) line shows that of CuO crystal. The quadrupole and dipole transitions occur at about 8979.5 eV and 8998.5 eV, respectively. The dashed vertical lines indicates the incident photon energies at which the measurements were taken.	61

4.3	The non-resonant inelastic X-ray scattering measurements of CuO at six different momentum transfer point. Surprisingly, at the zone boundary, $\xi = 1.00$, where the RIXS measurements are done, no inelastic signal was detected.	63
4.4	The open red circles with error bars show the center of mass of inelastic peaks that are obtained by fitting the spectra with three Lorentzian functions.	65
4.5	Individual scans of the RIXS measurements at the zone boundary, $\zeta = 1.0$. They are normalized with the incident number of photons. The y-scale has to be multiplied by 10^{-5} to get the cross-section per incident photon. The spectra are fitted by five Lorentzian peaks, the positions of the peaks are constrained so that the phonon peaks are at ~ 20 meV and ~ 40 meV. The intensities are also constrained so that they obey the detailed balance factor.	68
4.6	The red (square) symbols show how the ratio of the high-frequency phonon intensity to the overall integrated intensity changes as a function of incident energy. The blue (round) symbols show the change in the ratio of elastic signal to the overall integrated intensity.	69
A.1	Water lines are to cool the outer jacket of the oven for temperature stability. <i>Kapton</i> [®] polyimide film by <i>Dupont</i> TM is used for the front window. Two axis is enough to orient the crystal in the oven. Oven has a built in stage for horizontal axis rotation (tilt).	73
A.2	Top and side view. This is the part where the analyzer is actually placed. Set screws are to fasten the analyzer substrate.	75
A.3	The cover of the chamber. The window material is thin <i>Kapton</i> [®] polyimide film for minimum X-ray absorption. Feedthrough is also made in-house.	76
A.4	Stainless steel ring to lock the window.	77
A.5	Apparatus to use the heat exchange chamber in closed cycle displax refrigerators.	78
A.6	Apparatus to use the heat exchange chamber in a flow cryostat. . . .	79
A.7	Air is sealed in the chamber to guarantee temperature uniformity. . .	80

Images in this dissertation are presented in color

Chapter 1

Introduction

X-ray scattering has been a powerful tool in various branches of science since its discovery by Röntgen [9]. After an initial period of confusion about its exact nature¹, Barkla discovered the polarization of X-rays and demonstrated that they are in fact short-wavelength electromagnetic radiations [10]. Moseley convincingly showed that the emission lines from different elements are unique and such emissions can be used to identify these elements unambiguously [11]. Discovery of diffraction by von Laue and Bragg provided a powerful method to obtain information on the arrangement of atoms in crystals [12, 13, 14]. However, the dynamic behavior of atoms or electrons in relation to inelastic x-ray scattering was not known until Debye [15] and Compton [16].

The present research suggests a new experimental technique that measures vibrational spectrum of materials at an absorption edge of the material. This approach has the potential to further illuminate the dynamic behavior of atoms and electrons.

Four chapters cover the (1) background, (2) the design and construction of a new spectrometer, (3) its testing, and (4) its potential contribution. The present introductory chapter covers prior research on the relevant assessment techniques of dynamical be-

¹The reason it was called "X".

havior of atoms. Summarized are underlying principles of electromagnetic radiation and its interaction with matter. The second chapter presents relevant principles of crystal X-ray optics, the design parameters of an X-ray analyzer, and a step by step description of its construction. The third chapter describes how to use the spectrometer and initial tests of the instrument using a known sample. The fourth chapter demonstrates the use of the spectrometer to assess the vibrational spectrum of cupric oxide at the copper K-edge and reports the remarkable results.

1.1 The Importance of Inelastic X-ray Scattering and a Brief History

Debye calculated the temperature dependence of the diffraction pattern of crystals. The thermal movements of atoms could be observed via the reduced intensity of diffraction peaks expressed in the form of Debye-Waller factor [15, 17] which depends on the atomic vibrations around their equilibrium positions. Later, P. Olmer demonstrated that intensity of the diffuse scattering between the Bragg peaks can be used to reveal the dispersion relations of atomic vibrations [18]. Based on the earlier calculations by R. Weinstock [19], Brockhouse developed the inelastic neutron scattering technique and observed the energy distribution of the neutrons scattered from thermal vibrations [20, 21].

In inelastic neutron scattering (INS), a beam of neutrons with known energy (velocity) and direction is scattered from the sample and the scattered neutrons are collected as a function of energy and scattering angle. This way, frequencies of vibrational modes in the sample can be obtained along different directions in the reciprocal space. The energy scale of these vibrations are in the order of room temperature. Thermal neutrons with their few tens of meV energies match very well kinematically to this

kind of measurement. The strength of neutron scattering for this particular problem is the reason for the delay of inelastic x-ray scattering (IXS) technique to emerge and be recognized. Dorner and Burkel designed the first IXS instrument in 1986 and used it to measure vibrational spectra of light metals [22, 23, 24].

Figure 1.1 shows a few relevant techniques to measure the dynamical behaviors of materials in the frequency-momentum space. IXS can be a good alternative for the regions neutrons fail to cover. Another advantage of using X-rays over neutron scattering techniques is the relatively small beam size of X-rays. The X-ray beam can be further focused to micron levels for very small samples. A confined beam is also essential to study samples under pressure using pressure cells. For a comprehensive investigation of any elementary excitation, including phonons, spatial information can be obtained when the wavelength of the probe is in the order of inter-atomic distance. A typical inter-atomic distance of 1 \AA corresponds to the photon energies in the order of 10 keV . Measuring energy shifts in the order of 10 meV requires a resolving power of 10^6 . This is a non-trivial technical challenge and will be discussed in detail in Chapter 2.

If a beam of X-rays with known energy is scattered from a sample, the outgoing beam will contain X-ray photons with energies equal to or less than the incoming beam energy². If the measurements are taken with a moderate resolution, for a range that covers energy losses as high as 1 keV , the energy spectrum would look like the one in Figure 1.2 [1]³. Although this whole spectrum is a result of inelastic scattering of x-rays, historically IXS implies the low energy excitation part of this graph denoted as elastic scattering. With an instrument with better resolution, it can be seen that the elastic peak in this spectrum is composed of phonons, exciton

²This is true for zero sample temperature, for finite temperatures X-ray photons might gain energy by annihilating excitations.

³Instead of fixing the incident energy, Bowron et al. changed the incident energy and measured the photons at a fixed energy, this is another, actually the most common way of doing energy scanning. More details will be given in the subsequent chapters.

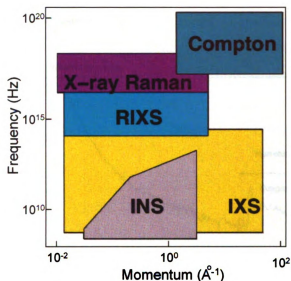


Figure 1.1: The accessible range for different spectroscopic techniques. The horizontal axis is the momentum range, which is important to probe the spatial dispersion of the excitations to be investigated. The vertical axis is the frequency, which is the energy divided by \hbar .

like charge excitations, plasmons and other low energy excitations as well as elastic signal. This is a good example to demonstrate the need for high resolution in X-ray spectroscopy.

The necessary resolution is today obtained by making use of Bragg reflection from perfect crystals. As it will be explained in more detail, later in Chapter 2, the problem associated with the instrumental resolving power has been solved to some extent. With the freedom of choosing X-ray energy, an IXS spectrometer with a resolution of 1 meV or better can be designed [25]. If there are requirements other than resolution, like the incident energy as in the case of resonant measurements, the design of a high-resolution instrument becomes more challenging. The main reason behind that is the lack of suitable crystals that have reflecting planes with sufficient efficiency at a restricted energy.

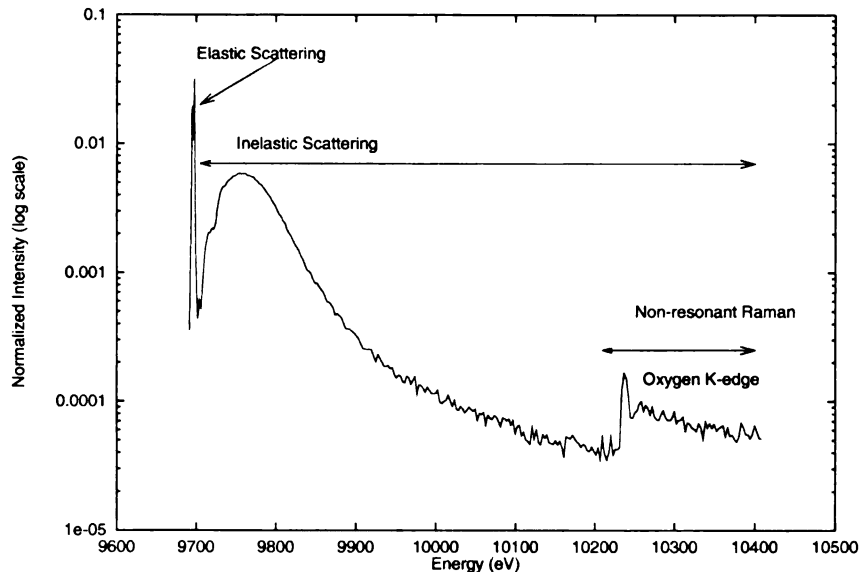


Figure 1.2: Inelastic scattering in the graph includes mainly the Compton scattering (big and ~ 200 eV-wide hump starting from ~ 9700 eV) and the Raman scattering (in this case, it is the Oxygen K-edge as the energy transfer is around 550 eV). Elastic scattering peak in this graph actually contains other inelastic scattering features but they are not visible due to low resolution (From ref. [1], reproduced with permission)

When the incident photon energy is tuned around an absorption edge of the material, an anomalous effect was first observed by Sparks [26]. Although this anomalous effect added more complexity in terms of cross-section and interpretation of the spectra, besides the instrumental challenges, the technique gained strength via intensity enhancement and element and excitation selectivity [27, 28, 29]. Resonant inelastic x-ray scattering (RIXS) technique proved to be useful in understanding collective charge excitations in transition metal oxides such as cuprates and manganites. The causes of instrumental difficulties in the case of restricted incident energy and the potential solutions will be discussed in the following chapter.

In this dissertation, the main goal is to find a new experimental method to measure vibrational spectra at an atomic resonance and demonstrate potential usage of such a technique. Since there was no existing experimental facility for such an experiment,

a new instrument had to be built. The next chapter is dedicated to the details of construction of this new instrument and the principles of crystal x-ray optics. The instrument is designed to operate at the copper K-edge because of the interest in cuprates due to high T_c superconductors (HTSC) [30]. Cupric oxide (CuO) was chosen as the sample for its structural, electronic, and magnetic similarities with HTSC cuprates.

1.2 Scattering Cross Section

Related with the phonon spectroscopy, the mechanism how the photons couple with nuclei can be answered within adiabatic approximation. Photons are quanta of electromagnetic waves and they directly couple with electrons. Since the electrons are two orders of magnitude faster than nuclei, they follow the instantaneous movement of the corresponding nuclei. The slow motion of atoms results in a change in electron density and it is detectable with x-rays⁴.

In order to construct the scattering cross section, it is better to start from the fundamental scattering unit, the electron. In the classical approximation, electrons are forced to oscillate by the electric field, E_{in} , of the incident radiation. As a result of this acceleration, electrons act like a dipole and emit radiation.

The vector potential experienced at a point separated from the electron by \vec{R} (Figure 1.3) is given by

$$\vec{A}(\vec{R}, t) = \frac{1}{4\pi\epsilon_0 c^2} \int_V \frac{\vec{J}(\vec{r}', t - |\vec{R} - \vec{r}'|/c)}{|\vec{R} - \vec{r}'|} d\vec{r}' \quad (1.1)$$

where ϵ_0 is the permittivity, c is the speed of light, and $\vec{J}(\vec{r}', t)$ is the current density of the source. Integration is taken over the volume that confines the charge distribution.

⁴For a more detailed review, the article by Eberhard Burkel is recommended [31].

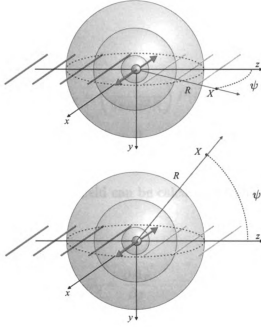


Figure 1.3: Top graph: the polarization (electric field) of the incoming wave is on the scattering plane. Bottom graph: the momentum transfer is perpendicular to the polarization of the incoming field (Figure reproduced from ref. [2]).

Here $|\vec{R}|$ is assumed to be much greater than both the oscillation amplitude of the electron and the wavelength of the radiation, λ . $|\vec{r}'|$ is negligible compared to $|\vec{R}|$ as a result of the first assumption. Thus,

$$\vec{A}(\vec{R}, t) \approx \frac{1}{4\pi\epsilon_0 c^2 R} \int_V \vec{J}(\vec{r}', t - R/c) d\vec{r}' \quad (1.2)$$

Current density, \vec{J} , is equal to the product of charge density ρ and the velocity \vec{v} ;

$$\int_V \vec{J} d\vec{r}' = \int_V \rho \vec{v} d\vec{r}' = \sum_i q_i \vec{v}_i = \frac{d}{dt} \sum_i q_i \vec{r}'_i \quad (1.3)$$

$\sum_i q_i \vec{r}'_i$ is the electric dipole moment P .

If the incident beam is linearly polarized along the x axis, the vector potential will also be along the x axis;

$$\begin{aligned} A_x &= \left(\frac{1}{4\pi\epsilon_0 c^2 R} \right) \dot{P}(t') \\ A_y &= A_z = 0 \end{aligned} \quad (1.4)$$

The components of the magnetic field can be calculated from $\vec{B} = \vec{\nabla} \times \vec{A}$

$$B_x = 0 \quad B_y = \frac{\partial A_x}{\partial z} \quad B_z = -\frac{\partial A_x}{\partial y} \quad (1.5)$$

$$\begin{aligned} \frac{\partial A_x}{\partial z} &= \left(\frac{1}{4\pi\epsilon_0 c^2} \right) \frac{\partial}{\partial z} \left(\frac{P(t')}{R} \right) \\ &= \left(\frac{1}{4\pi\epsilon_0 c^2 R} \right) \left[\frac{1}{R} \frac{\partial \dot{P}(t')}{\partial z} - \frac{\dot{P}(t')}{R^2} \frac{\partial R}{\partial z} \right] \end{aligned} \quad (1.6)$$

since we are interested in the far-field limit of B, i.e. R is much greater than the oscillation amplitude, we can neglect the second term

$$B_y = - \left(\frac{1}{4\pi\epsilon_0 c^2 R} \right) \frac{1}{cR} \ddot{P}(t') \left(\frac{z}{R} \right) \quad (1.7)$$

$$\vec{B} = \left(\frac{1}{4\pi\epsilon_0 c^2 R} \right) \frac{1}{cR} \ddot{P}(t') \times \hat{R} \quad (1.8)$$

$$\ddot{P} = q\ddot{x} \quad (1.9)$$

\ddot{x} is acceleration and is equal to the force exerted on the electron divided by its mass so that Eqn. 1.9 can be rewritten as

$$\ddot{P} = q \frac{qE_{in}}{m} = \frac{q^2}{m} E_0 e^{-i\omega(t-R/c)} \quad (1.10)$$

Substituting 1.10 in 1.8 and using the identity $|E| = c|B|$, electric field strength can be represented as

$$E(t) = - \left(\frac{e^2}{4\pi\epsilon_0 mc^2} \right) \left(\frac{e^{ikR}}{R} \right) E_{in}(t) \cos \psi \quad (1.11)$$

where ψ is the angle between the position vector \vec{R} and the polarization of the incident photon wave, i.e. direction of the incident electric field (see Figure 1.3). $\left(\frac{e^2}{4\pi\epsilon_0 mc^2} \right)$ is the Thomson scattering length, r_0 , which is also known as the classical electron radius. The minus sign indicates that there is a phase shift of π between the incident and the scattered fields.

Differential cross-section is defined by the power scattered into the solid angle $d\Omega$ normalized by the incident flux. The power per unit area is proportional to $|E|^2$.

$$\frac{d\sigma}{d\Omega} = r_0^2 \cos^2 \psi \quad (1.12)$$

The scattering from an atom can be calculated by the interference of the scattering from individual electrons that belong to the atom. The phase difference between the two volume elements is the scalar product of the two vectors \vec{k} and \vec{r} , where \vec{k} is the wave vector of the incident field and \vec{r} is the vector between the two infinitesimal volume elements. The phase difference between the scattered radiation from the two volume elements is $-\vec{k}' \cdot \vec{r}$, then the resulting phase difference is $(\vec{k} - \vec{k}') \cdot \vec{r}$. Where

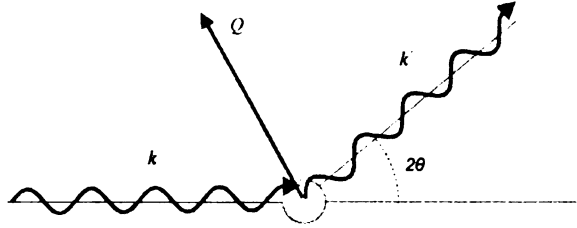


Figure 1.4: A general scattering geometry, where k is the wave vector of the incoming beam and k' is that of the scattered beam with a scattering angle of θ .

$(\vec{k} - \vec{k}')$ is defined as \vec{Q} , wave vector transfer, i.e. momentum transfer divided by \hbar .

A general scattering event can be shown schematically as in Figure 1.4. When the scattering is elastic, i.e. $|\vec{k}| = |\vec{k}'|$, $|Q| = 2|k| \sin \theta = (4\pi/\lambda) \sin \theta$.

A volume element d^3r at r will contribute an amount $-r_0\rho(r)dr$ to the scattered field with phase factor of $e^{i\vec{Q}\cdot\vec{r}}$. The total scattering length of the atom is then

$$-r_0f^0(Q) = -r_0 \int \rho(r)e^{i\vec{Q}\cdot\vec{r}}dr \quad (1.13)$$

where $f^0(Q)$ is known as the atomic form factor. For forward scattering, $Q \rightarrow 0$, all the volume elements scatter in phase so that $f^0(Q) \rightarrow Z$, the number of electrons in the atom. Electrons in the core shells are bound to the atom which is regarded as stationary. For photon energies less than binding energy, electrons cannot be assumed to be free. Even for high energy photons due to the binding of electrons, the scattering length is reduced by some amount f'^5 . For the extreme case of very high energy photons f' goes to zero. The derivation started with the forced oscillation approximation of electrons. There will be dampening of these oscillations that appears as a phase lag. This effect can be introduced as if'' which represents the dissipation in the system. The atomic form factor is then

⁵ f' should not be confused with the derivative of f . It is a common notation to show the dispersion corrections to atomic form factor.

$$f(\vec{Q}, \omega) = f^0(\vec{Q}) + f'(\omega) + if''(\omega) \quad (1.14)$$

Scattering from a collection of atoms, assuming the same type of atoms and the unit cell consists of one atom, can be calculated as the summation of individual atoms with a phase difference, $\vec{Q} \cdot \vec{R}_n$, where \vec{Q} is again the wave vector transfer and \vec{R}_n is the vector connecting the atoms. The sum will be in the order of the number of unit cells when

$$\vec{Q} \cdot \vec{R}_n = 2\pi \times \text{integer} \quad (1.15)$$

otherwise the summation will be of order unity.

When the wave vector transfer is equal to the reciprocal lattice vector, the lattice sum of the scattering factor will not be vanishing. This is another way of explaining the *Bragg Law*.

Construction of the differential cross-section was mainly concerned with the direction of the scattered radiation and the resulting wave vector transfer. When the inelastic case is also taken into consideration the cross-section should contain the frequency dependence. The double differential cross-section can be derived from the Kramers-Heisenberg formula [32] and represented as

$$\frac{d^2\sigma}{d\Omega d\omega} = \frac{d\sigma}{d\Omega} S(\vec{Q}, \omega) \quad (1.16)$$

where the first term on the right hand side is the overall scattering factor derived above, and $\hbar\omega = E_f - E_i$ is the energy transfer to the system from initial energy E_i to the final energy E_f . The second term depends on the dynamics of the particles in the scattering volume, and its quantum mechanical representation is given by

Table 1.1: The high-resolution IXS spectrometers with meV -resolution available as user facilities

Location	Reflection	Energy (keV)	ΔE (meV)	Q Transfer Range (nm^{-1})
SPring-8, Japan	Si(n n n)	15.816 – 21.747	6.0 – 1.5	1 – 101
APS, USA	Si(18 6 0)	21.657	2.2	1 – 34
	Si(12 12 12)	23.724	1.6	1 – 70
ESRF, France	Si(n n n)	13.840 – 25.704	7.6 – 1.0	1 – 120

$$S(\vec{Q}, \omega) = \sum_{i,f} g_i |\langle i | \sum_j e^{i\vec{Q}\cdot\vec{r}_j} | f \rangle|^2 \delta(\omega - \omega_f + \omega_i) \quad (1.17)$$

where summation is over all electrons, and g_i is a weight factor for the initial states. This can be expressed as a time Fourier transform of the density correlation function;

$$S(\vec{Q}, \omega) = \frac{1}{2\pi} \int dt (e^{-i\omega t} \sum_i g_i |\langle i | \sum_{j,l} e^{i\vec{Q}\cdot\vec{r}_j(0)} e^{i\vec{Q}\cdot\vec{r}_l(t)} | i \rangle|) \quad (1.18)$$

For coherent elastic scattering where $\omega = 0$, the cross-section is reduced to $S(Q) = |\sum_j e^{i\vec{Q}\cdot\vec{r}_j}|^2$. The sum is non-vanishing only for $\vec{Q} \cdot \vec{r}$ is an integer multiple of 2π , which is the case for Bragg scattering as mentioned above.

With a coherent inelastic x-ray scattering, we can observe the electron density change. As mentioned earlier, in the adiabatic approximation this gives the information about the atomic vibrations, i.e. phonons.

In order to measure phonons, one needs a spectrometer with a resolution in the order of the phonon energies and a wave vector that can provide spatial information of the phonon. X-rays with 10 keV and ~ 5 meV resolution meet these criteria. Inelastic X-ray scattering (IXS) measurements have been used to address problems related to dynamical properties of atoms or molecules in condensed matter for more than two decades. Table 1.1 shows a brief summary of the parameters of the spectrometers that are currently available as a user facility.

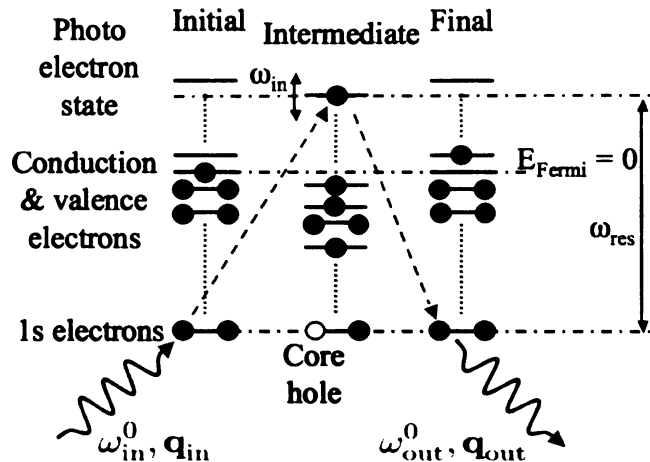


Figure 1.5: Schematic representation of RIXS processes. Photon with frequency ω_{in}^0 excites a 1s electron to a 4p state. The core-hole potential *shakes-up* the system and causes excitations (it is an electron-hole pair in this case) in the valence states (for cuprates, it is the hybrid level of Cu-3d and O-2p). The excited electron fills the core-hole by emitting a photon with a frequency equal to the frequency of the incoming photon minus the expense of the excitation. Figure reproduced from ref. [3] with permission.

1.2.1 Resonant Inelastic X-ray Scattering with Momentum Resolution

So far no assumption about the incident photon energy has been made while deriving the scattering cross-section. When the incident photon energy is tuned around an absorption edge of the atom, a core level electron is excited to an unoccupied upper level. There are several ways for this excited atom to relax back to ground state. The excited electron can return to its original position by emitting a photon with the same wavelength the electron initially absorbed. This process is said to be resonant elastic. Resonant emission happens when one of the lower level electrons, instead of the excited electron, fills up the core hole.

The focus of RIXS, on the other hand, is the quasi-elastic scattering process where

the excited electron decays back to the original core level after inelastically coupling with the system. Figure 1.5 shows a schematic representation of the RIXS process [3]. The strong perturbation due to the core-hole potential causes various excitations like orbitons, magnons, electron-hole pairs, etc. As seen in the figure, the excitations are created during the intermediate state and the types of excitations depend on what kind of intermediate state is created. Intermediate state depends on the incident photon energy. By tuning the incident energy around the absorption edge, different excitations can be enhanced selectively. This feature is a strength of the technique together with the site selectivity [33].

Eqn. 1.16 is only the first term in the Kramers-Heisenberg [32] formula as the quadratic term is negligible unless the incident radiation energy is equal to an absorption energy of the atom. The second term of the Kramers-Heisenberg formula that becomes dominant for the so called resonant case is

$$\frac{d^2\sigma}{d\Omega d\omega} = const \sum_f \left| \sum_n \frac{\langle f|H_{int}|n\rangle\langle n|H_{int}|i\rangle}{\hbar\Omega - \hbar\omega_{res} - i\Gamma} \right|^2 \quad (1.19)$$

where i, n, and f denote the initial, intermediate, and final states, respectively. H_{int} is the interaction Hamiltonian. $\hbar\Omega$ is the incident photon energy and $\hbar\omega_{res}$ is the resonant absorption energy. Γ is the lifetime of the core hole.

RIXS has been a useful tool in obtaining information on the electronic structures in correlated electron systems [34, 35]. The elementary excitations that are studied with RIXS are in the order of eV or less and the incident photon energy for K-edges is 5 to 10 keV. The instrumental details will be given in the following chapters, however it is worth mentioning that when the incident photon energy is restricted, the design and construction of a spectrometer become a real challenge. This is the reason the existing K-edge RIXS spectrometers has resolution of 100 meV or higher⁶.

⁶Table 1.2 shows the non-resonant spectrometers.

L-edge and M-edge RIXS measurements are also possible, however there are other technical problems associated with the low incident photon energy that need to be addressed. First of all K-edge measurements have bulk sensitivity due to the relatively high energy X-rays. On the other hand L- and M-edge measurements are highly surface sensitive that they require rigorous sample preparation. Sample has to be placed in a very high vacuum for these relatively low energy X-ray measurements due to air absorption. Another drawback of L- and M-edge experiments is the limited momentum transfer capability. It is practically impossible to cover the full Brillouin zone in most cases. As it will be mentioned in chapter 2, perfect crystals are employed as natural slits to monochromatize the X-ray. In case of low energy X-rays atomic spacings are too fine whereas artificial slits are too coarse for intended quality of monochromaticity.

Designing and constructing a spectrometer at the copper K-edge was a critical part of this dissertation. The new analyzer has improved the resolution by a factor of almost three. This new capability made it possible to make an attempt to measure the phonon excitations at the K-edge energy of copper.

1.3 Studies on Cupric Oxide (CuO)

Cupric oxide (CuO) has a tenorite structure, which has monoclinic symmetry with space group $C2/c$ [36]. The samples were grown by the Dresden group⁷ from mechanically pressed and heat treated CuO powder in a floating zone facility with radiation heating under elevated oxygen pressure [37]. By doing so, they achieved better control over the stoichiometry and bigger single crystals. The lattice parameters of the monoclinic CuO are $a = 4.6858(1) \pm 0.0003\text{\AA}$, $b = 3.4252(1) \pm 0.0002\text{\AA}$, $c = 5.1308(2) \pm 0.0003\text{\AA}$ and $\beta = 99.519(2)^\circ \pm 0.003^\circ$.

⁷G. Behr, M.-O. Apostu, and N. Wizent, IFW Dresden, Germany

CuO single crystal has been studied extensively due to the renewed interest in HTSC. Although its structure is quite different than that of the HTSC cuprates, CuO has two ribbon-like plackets running along $(1\ 1\ 0)$ and $(1\ -1\ 0)$ (see Figure 4.1). Copper coordinated with four oxygen atoms forming a plane similar to those in HTSC cuprates. The fact that superconductivity occurs along CuO_2 planes has stimulated extensive research activities focused on these planes.

In this dissertation, phonon spectrum of cupric oxide is measured at the copper K-edge. It is intended to show that the inelastic x-ray scattering measurements at an absorption edge has potential as one more tool for a better understanding of both the interaction of x-ray photons with lattice excitations and the nature of electron-phonon coupling in correlated electron systems.

Chapter 2

Spectrometer Design

2.1 Perfect Crystals as Monochromators and Dynamical Theory

In analogy to the diffraction of visible light from slits, atoms located periodically on a lattice can be thought of as a three-dimensional grating. A monochromatic electromagnetic plane wave with wavelength comparable to the inter-atomic distance (X-radiation), after being scattered from a crystal, forms a diffraction pattern as a function of momentum transfer. Maxima occur when the momentum transfer vector is equal to a reciprocal lattice vector. In other words, when the path difference of two waves from two different scattering centers (atoms or atomic planes) is equal to an integer multiple of the incoming field's wavelength (Figure 2.1), the phase difference between the two waves yields a constructive interference. The analysis of this diffraction pattern provides information on the arrangement of atoms [13, 14]. Since the inter-atomic distance is in the order of \AA , the photon energy that corresponds to this wavelength is in the order of keV .

This approach neglects both absorption and extinction. Therefore it is valid only

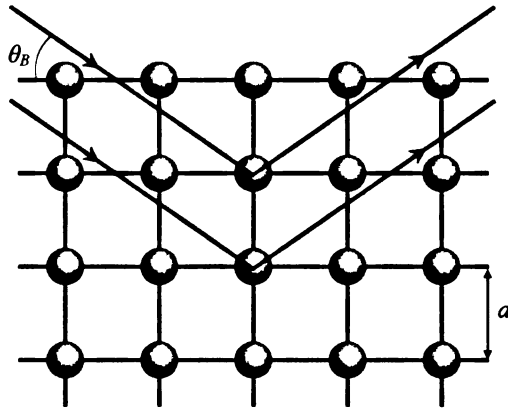


Figure 2.1: The inter-atomic spacing is d and the condition for Bragg diffraction is $n\lambda = 2d\sin\theta$. n is an integer, equal to 1 for the first harmonics and will be omitted during the subsequent discussion.

in the case of very small crystals where these two factors are relatively small and surface effects are negligible¹. Normal absorption can be taken into account by an exponential factor, $e^{-\mu x}$ where μ is the linear absorption coefficient and x is the path length X-radiation traveled in the crystal.

The extinction is the result of the interaction of the incident and scattered radiation. The electric field in the crystal makes a contribution to the incident wave field. This crystal field depends on the diffracted waves, which depend on the internal incident waves. This is the reason the general theory of diffraction in crystals is called the *dynamical theory*.

In the interest of brevity, the complete derivation of the theory will be omitted as it is covered in many basic text books [38, 39, 40]. Instead, a summary and a few findings, particularly relevant to the present research, will be discussed. It is worth mentioning that at every layer of the crystal small but a finite portion of the incident wave is reflected and the transmitted wave has a small phase difference. That is why

¹Only the surface where X-ray is glancing matters.

the reflected beam parameters heavily depend on how much the beam penetrated in the crystal.

Reflectivity of a semi-infinite crystal can be represented as

$$R = \left| \frac{\chi_H}{\chi_{\bar{H}}} \right| \left| -y \pm \sqrt{y^2 - 1} \right|^2 \quad (2.1)$$

where χ_H is the Fourier component of the crystal's electric susceptibility, which is defined as the ratio of polarization caused by an applied electric field to the electric field strength. H is the reciprocal lattice vector of the crystal for a given reflection, “-” on top of H denotes $-H$ and $\chi_H = \chi_{\bar{H}}$ for centrosymmetric crystals. χ_H can be defined as

$$\chi_H = -r_e \frac{\lambda^2}{\pi V} F_H \quad (2.2)$$

where r_e is the classical electron radius and F_H is the structure factor of the unit cell with volume V . F_H is the sum of the atomic form factors for each element that make up the unit cell with corresponding phase differences $e^{i\vec{H} \cdot \vec{\tau}_n}$ and Debye-Waller contribution $e^{-W_n(H)}$.

$$F_H = \sum_n f_n(H) e^{i\vec{H} \cdot \vec{\tau}_n} e^{-W_n(H)} \quad (2.3)$$

Atomic form factor, $f_n(H) = f_n^0(H) + f_n'(\lambda) + i f_n''(\lambda)$, includes the dispersion corrections as in Eqn. 1.14. e^{-W_n} is the square root of the Debye-Waller factor which is related to thermal vibrations of the atoms.

As will be mentioned later, for a highly symmetric crystal structures there is higher chance for the structure factor to vanish. Having more than one type of atom in a less symmetric unit cell increases the number of unique allowed Bragg reflections.

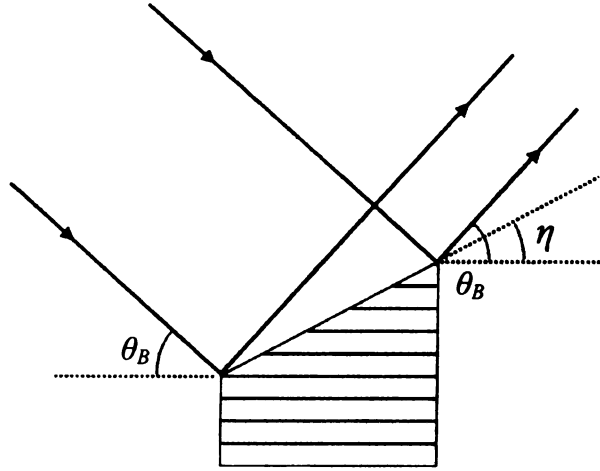


Figure 2.2: An asymmetric crystal with the asymmetry angle of η

For $-1 \leq y \leq 1$ reflectivity will have its maximum value and decay very fast outside of this range, which is called the region of total reflection. The parameter y in Eqn. 2.1 can be written as

$$y = \frac{\chi_0(1 - b) + \alpha b}{2\sqrt{C^2|b|\chi_H\chi_{\bar{H}}}} \quad (2.4)$$

where χ_0 can be calculated from Eqn. 2.2 for $H = 0$ and b is the asymmetry factor

$$b = -\frac{\sin(\theta_B - \eta)}{\sin(\theta_B + \eta)} \quad (2.5)$$

where θ_B is the Bragg angle and η is the angle between the Bragg planes and the physical reflecting surface of the crystal. b is equal to -1 for the symmetric case (Figure 2.2) and exact back-scattering where θ_B is equal to 90° .

C is the polarization parameter, which is equal to the vector product of the unit vectors in the direction of electric field of the incident beam and the momentum

transfer. C is equal to 1 for the σ -geometry, where the electric field is perpendicular to the scattering plane and $\sin 2\theta$ for the π -geometry, where the electric field is parallel to the scattering plane.

The exact expression for the parameter α is [41]

$$\alpha = 4 \sin \theta_B [\sin \theta_B - \sin \theta] \quad (2.6)$$

which can be expressed in terms of either the incident angle, θ , or the energy, E to track the reflectivity variation around the Bragg angle, θ_B , or Bragg energy E_B , respectively.

Assuming that the angular variation and the energy variation are small, i.e. $|\delta\theta| = |\theta_B - \theta| \ll 1$ and $|\epsilon| \equiv |(E - E_H)/E_H| \ll 1$, α can be expressed approximately as

$$\alpha = 2[\delta\theta^2 - 2\epsilon] \quad (2.7)$$

Extinction length is the depth at which the X-ray intensity is reduced by $1/e$, assuming there is no absorption. In order for the reflectivity to build up and the bandwidth to be defined, the crystal needs to extend a few extinction length, which is estimated to be minimum $2\pi\tau$ [42], where τ is the extinction length. Otherwise interference from the back surface of the thin crystal would make a contribution to the reflected beam.

At the center of the total reflection region, the extinction length takes its maximum value;

$$\tau(0) = \frac{\gamma_0}{K|C\chi_H|\sqrt{|b|}} \quad (2.8)$$

where $\gamma_0 = \sin(\theta - \eta)$ and K is the amplitude of the momentum transfer vector.

Spectral width of a Bragg reflection is

$$\frac{\Delta E}{E} = \frac{|C\chi_H|}{\sin^2 \theta \sqrt{|b|}} \quad (2.9)$$

By using Eqn. 2.8 for the symmetric case, the relative bandwidth can be rewritten as

$$\frac{\Delta E}{E} = \frac{d_H}{\pi\tau(0)} \quad (2.10)$$

According to this expression, for a given reflection, spectral width depends only on the extinction length and the d-spacing, d_H . For maximum absolute resolution, ΔE , for a given Bragg reflection, the energy of the photon beam, E , should be minimum. This is one of the consequences of exact back-scattering since for a given Bragg case λ takes its maximum value for $\theta_B = 90^\circ$.

Angular acceptance, or the Darwin width, is the full width at half maximum (FWHM) of the reflectivity profile when the energy, E is fixed at the Bragg energy, E_B and the angle, θ is varied around the Bragg angle, θ_B .

$$\Delta\theta = \frac{\Delta\alpha}{2 \sin 2\theta} = \frac{2|C\chi_H|}{\sin 2\theta \sqrt{|b|}} \quad (2.11)$$

Clearly, $\Delta\theta$ increases dramatically as θ approaches to 90° . This is the main advantage of back-scattering geometry that, at or close to back-scattering, the reflection becomes less susceptible to the angular variations. However this expression is not valid for exact back-scattering case. For the exact back-scattering case the angular acceptance can be calculated as [40]

$$\Delta\theta = \sqrt{\Delta\beta} = 2\sqrt{|C\chi_H|} \quad (2.12)$$

By using Eqn. 2.9, Eqn. 2.11 can be rewritten in terms of relative spectral bandwidth as

$$\Delta\theta = 2\sqrt{\frac{\Delta E}{E}} \quad (2.13)$$

For an energy resolution of 1 *meV* using 10 *keV* X-ray photons, $\Delta\theta$ would be in the order of *mrad*. It brings great ease to the X-ray optics design since even a beam with a divergence in the order of *mrad* satisfies the Bragg condition.

2.2 Instrumentation Related to Inelastic X-ray Scattering

A typical inelastic X-ray spectrometer is shown in Figure 2.3. The main function of the set of instruments preceding the sample is to provide an intense photon beam with a known energy and direction. The undulator is the first equipment to produce and to tune the X-ray energy. Then the water-cooled, double crystal pre-monochromator filters the beam from the insertion device, taking much of the power. A secondary, high-resolution monochromator further reduces the bandwidth. If needed, a focusing mirror is located after the monochromators to confine the beam to a very small area for special needs like samples under pressure.

The secondary (high resolution) monochromator consists of a pair of channel-cut Si crystals, which guarantees four reflections, i.e. the first and fourth surfaces are part of the same channel-cut crystal and rotated together, same holds for the second and third reflections (Figure 2.4).

Since the very first days of x-ray spectroscopy, lack of intensity has been one of the

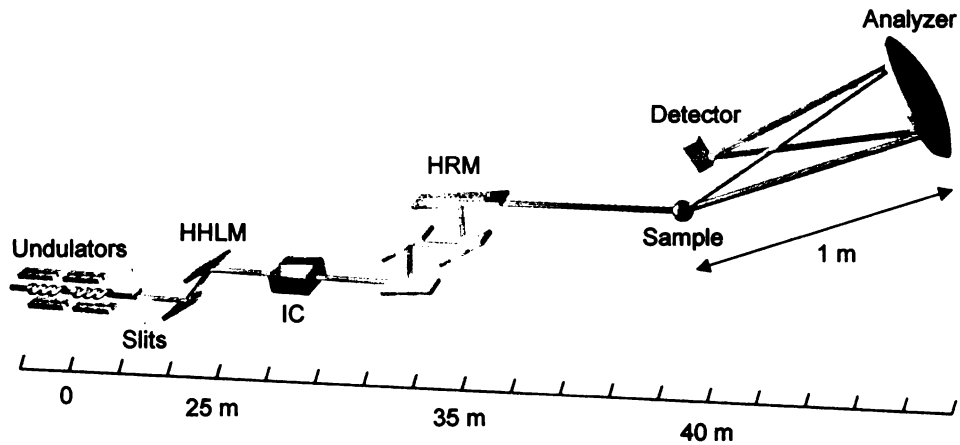


Figure 2.3: A typical IXS spectrometer at a synchrotron. Here are the specific details for the test experiments at station 30 ID at the Advanced Photon Source: **Undulator**: 2-in-tandem, 3.0 cm period, each 2.4 m long, **HHLM**: High Heat Load Monochromator, C (1 1 1) double crystal diamond, **IC**: Ion Chamber to count the number of incident photons for normalization purposes, **HRM**: High Resolution Monochromator, Si (4 4 4) in nested geometry, **Analyzer**: Al_2O_3 (0 4 14) diced, spherically bent crystal analyzer, **Detector**: Solid state diode detector

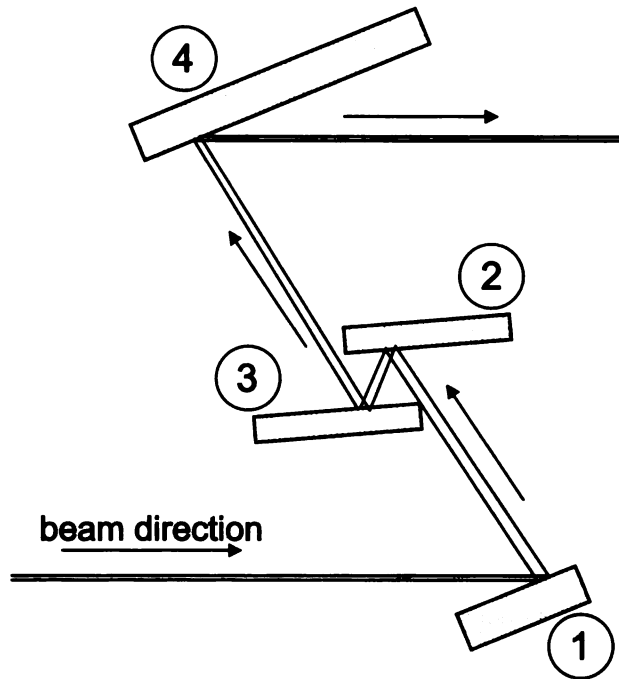


Figure 2.4: The first and the fourth surfaces are made by cutting a channel from a single piece of crystal, the second and the third are another channel cut.

biggest challenges during these flux-hungry experiments² [43]. The advent of synchrotron radiation has significantly improved the experimental conditions by making intense monochromatic beams more readily achievable. The current difficulty is primarily in achieving high efficiency in analyzing the inelastically scattered photons and counting them. The second section after the sample is mainly dedicated to solve this problem. Naively, one may suggest to place a detector to collect the scattered photons. However, there is no X-ray detector to provide a resolution of 100 *meV* or better. Therefore, just like monochromators, perfect crystals have to be used to analyze the scattered beam. However, unlike the monochromator, the analyzer has to accept radiation spherically scattered from a point-like sample. The problem can be summarized as the difficulty to collect photons of a narrow bandwidth scattered from a point source, and analyze its energy spectrum efficiently.

The method of choice would be employing the Rowland circle geometry [44]. If the reflecting boundary of the crystal is curved with a radius R and the atomic reflecting planes are bent to the radius $2R$, any point source on the Rowland circle will have an image on the very same circle [43]. It is impractical to cut and bend the analyzing crystal with such high accuracy. Moreover it is not necessary. If the size of the analyzer is small compared to the radius of curvature, to a good approximation, the reflecting boundary of the crystal can coincide with the atomic reflecting planes. Therefore, as a practical solution, spherically bent analyzers are used to satisfy the same Bragg condition at every point on the analyzer surface [22, 31, 45]. Thus, all the rays diffracting from the analyzer are focused to a point. A good focus can be achieved on a detector spot when the sample, the analyzer, and the detector are placed on a Rowland circle, the diameter of which is equal to the radius of curvature of the analyzer.

²“The limiting factor in many research problems in X-ray spectroscopy today is found in the difficulty of obtaining the necessary intensity.” Jesse W. DuMond, 1930

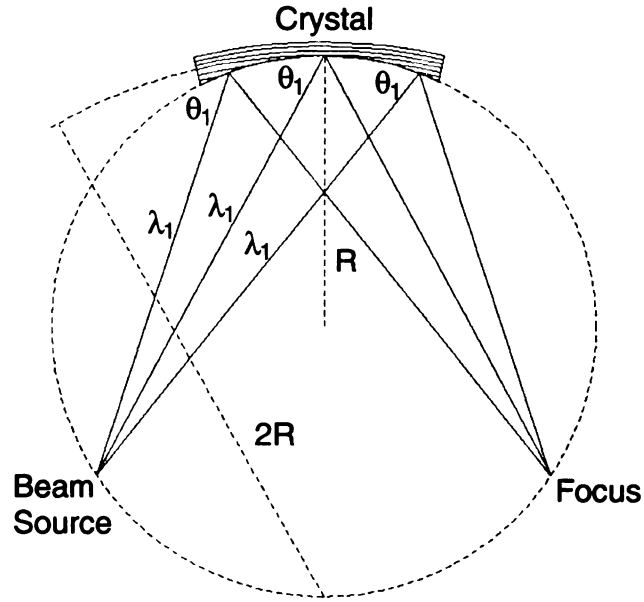


Figure 2.5: Rowland circle. A source on any point on the circle has a focal point on the same circle.

Bending a crystal wafer introduces stress due to elastic deformation of lattice planes, which broadens the bandwidth [46, 47, 48]. Regardless of the intrinsic energy resolution of the crystal, bending of a wafer introduces substantial energy broadening. The contribution due to the bending is [49]

$$\frac{\Delta E}{E} = \frac{2t\mu}{R(1-\mu)} \quad (2.14)$$

where μ is the Poisson number of the crystal, t is the penetration depth of X-rays, and R is the bending radius. For example, Poisson number for silicon is 0.17. This gives around 1 eV energy broadening at 10 keV X-rays, for a wafer bent to a 1 m radius. For penetration depth, t , $2\pi\tau$ is a good approximation [42], where τ is the extinction length for a given reflection.

In order to avoid the energy broadening and to keep the lattice periodicity undis-

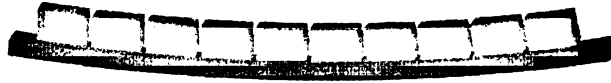


Figure 2.6: An illustration of a row of pixels. Individual flat and stress-free crystal pieces make up the spherical surface.

turbed, crystal wafers need to be diced and mounted on a spherical plane (Figure 2.6) so that stress-free flat crystal pixels make a mosaic spherical surface. The energy resolution of the analyzer would then vary with the size of the pixel because the Bragg angles on two extreme points of a single flat pixel differ by an amount that depends on the size of the pixel and its distance from the scattering center [31] (see Figure 2.7). The bandwidth contribution due to this effect can be approximated as

$$\frac{\Delta E}{E} = \frac{p}{L} \cot \theta \quad (2.15)$$

where p is the size of a single pixel, L is the distance of the pixel to the source, and θ is the Bragg angle. Note that this expression is not valid for the exact back-scattering case which will be discussed in the section about geometrical contributions. Here the emphasis is on the intrinsic tolerance to angular variations for a given Bragg case.

This tolerance is proportional to the intrinsic angular acceptance of a crystal and is larger when the Bragg angle is very close to 90° (Figure 2.9). This makes it advantageous to design an analyzer that operates at or very close to back-scattering.

2.2.1 Angular Acceptance

The use of back-scattering geometry dates back to late 1920s. van Arkel (1927) and later Sachs and Weert (1930) performed measurements to determine lattice parameters and elastic stress in crystals. They employed Bragg reflections close to 90° to

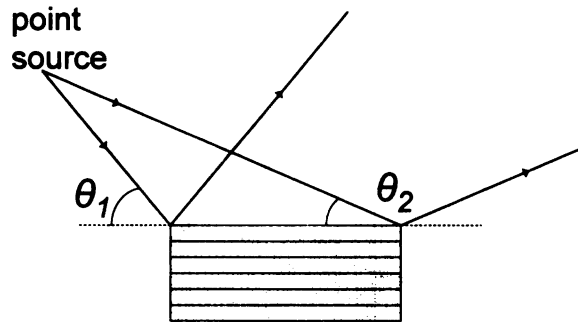


Figure 2.7: Bragg reflection is for plane waves (point source at infinitely large distance). For the case of spherical waves, the glancing angle for the incident beam at two different point on a crystal surface is not equal. This angular variation contributes to the energy bandwidth.

improve precision and reduce errors. In 1982, Graeff and Materlik succeeded utilizing back-scattering for inelastic x-ray studies in a synchrotron.

According to Eqn. 2.10 the relative resolution, $\Delta E/E$, does not depend on angle. For back-scattering condition, the Bragg equation, $\lambda = 2d \sin \theta$ suggests that the energy takes its minimum value for a given reflection with fixed lattice spacing, d . Since the relative resolution is a constant of a given lattice spacing, the absolute bandwidth, ΔE takes its minimum value for θ equal to 90° .

As already mentioned, the angular acceptance takes its highest values at angles close to back-scattering and the energy susceptibility to angular variations becomes minimum (see Figure 2.8). Its value drops very fast as the angle starts moving away from 90° (Figure 2.9). This fact forces two constraints to a high-efficiency diced-mosaic crystal analyzer; the analyzer has to be as close to back-scattering as possible and it should stay there.

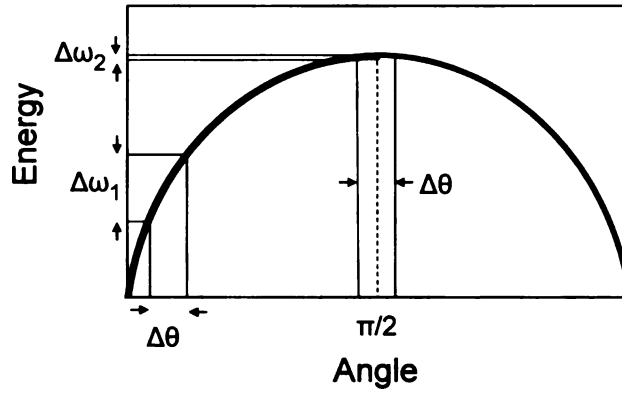


Figure 2.8: Graphical representation of Bragg equation. For the same $\Delta\theta$ the energy variations are shown at two different Bragg angles.

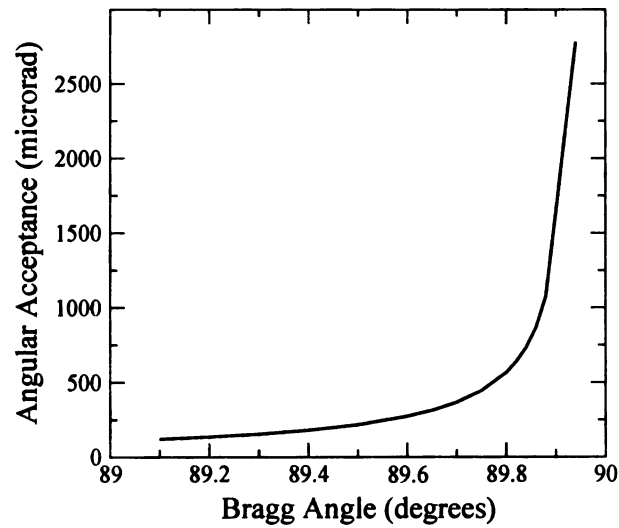


Figure 2.9: Intrinsic angular acceptance for a given Bragg reflection increases as the Bragg angle approaches to 90° .

2.2.2 Geometrical Contributions and Demagnification

By differentiating the Bragg law, the relative variation of the wavelength can be expressed as

$$\frac{\delta\lambda}{\lambda} = \cot\theta \delta\theta \quad (2.16)$$

for $\theta = \pi/2 - \xi$, where ξ is the deviation from back-scattering geometry, $\cot\theta\delta\theta$ can be written as $\tan\xi\delta\xi$. For small ξ , $\tan\xi$ can be replaced by ξ . Thus,

$$\frac{\delta E}{E} \approx \xi \delta\xi \quad (2.17)$$

Note that $\delta\lambda/\lambda$ is equal to $\delta E/E$.

The geometrical contribution to the energy resolution takes its minimum value when the deviation from the back-scattering geometry, ξ is minimal. Even at exact back-scattering there is a finite angular variation due to the divergence of the beam.

Exact back-scattering, i.e. $\xi = 0$, requires semi-transparent detector and time resolution to distinguish the beam scattered from the sample from the analyzed beam from the analyzer³. This geometry also requires the detector and the sample to be at the same location, which is another problem.

The analyzer works like a focusing mirror so the equation for concave mirrors is valid (see Figure 2.10);

$$\frac{1}{L} + \frac{1}{l} = \frac{2}{R} \quad (2.18)$$

where R is the bending radius of the mirror (analyzer). L is the distance between

³Note that even for this case the geometrical contribution is not zero due to the finite divergence of the beam.

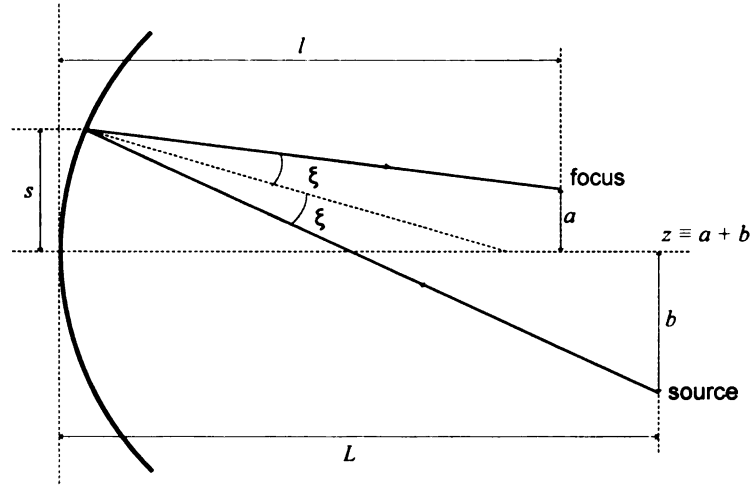


Figure 2.10: A focusing mirror can be thought of as a concave mirror as the demagnification relations are identical.

the source (sample) and the mirror (analyzer), and l is the distance from mirror (analyzer) to the focal point (detector). In order to prevent the detector from the scattered beam the detector is located away from the beam path, a conical region from the sample to analyzer, which gives a tangential displacement of z . For $z \ll R$, the deviation from the back-scattering geometry can be calculated as

$$\begin{aligned}
 2\xi &= \frac{s - z/2}{l} - \frac{s + z/2}{L} \\
 \delta\xi &= \frac{S}{2L} \left(\frac{L}{l} - 1 \right)
 \end{aligned}
 \tag{2.19}$$

where s is the distance of the reflecting point from the center of the analyzer. For the last step, variation in s is replaced by the size of the analyzer, S . Then the energy resolution contribution can be calculated by using Eqn. 2.17. Since in mirrors the ratio L/l is called the demagnification, the geometrical contribution just derived is also called the demagnification contribution.

2.2.3 Energy Scanning

For non-resonant inelastic X-ray scattering measurements, where there is no restriction on the incident energy, the energy scanning can be done by changing the incident energy and keeping the analyzer energy constant. This method does not disturb the back-scattering arrangement and it has been used for non-resonant IXS at the current facilities (Table 1.1). However if the incident energy has to be restricted to a value like an absorption edge as it is the case for resonant inelastic X-ray scattering (RIXS) measurements, the energy scanning has to be performed by changing the analyzer's energy. To change the energy (or wavelength) for a given reflection, the diffraction angle θ or the lattice spacing d has to be changed (recall the Bragg's equation, $\lambda = 2d \sin \theta$). Changing the angle of the analyzer to scan the energy would push the analyzer far away from its 90° Bragg condition and sacrifice the advantages of back-reflection. Therefore one has to think about changing the lattice spacing, i.e. temperature scanning. The expression for the energy variation can be derived by using the Bragg equation and the expression for the linear thermal expansion, $\Delta d = d\alpha\Delta T$ as the length changes linearly with the thermal expansion coefficient α . Keeping everything else constant, the variation in energy is

$$\Delta E = E\alpha\Delta T \quad (2.20)$$

For a typical crystal, the linear thermal expansion coefficient is in the order of 10^{-6} at room temperature, drops monotonically to zero as the temperature decreases. For energy scanning purposes, the higher limit of the energy is defined by the temperature at which the thermal expansion coefficient becomes zero as further change in the temperature would have any effect neither on the lattice spacing nor on the energy (Eqn. 2.20). The lower limit of the energy is in principle determined by the melting of the crystal. However, in practice, other instrumental factors like the materials used

to house the equipment or the glue to keep them together partly define the upper temperature limit, and therefore the lower limit of the energy. In practice a scan range of ~ 20 eV is achievable.

Energy scanning has been performed on back-scattering monochromators at the ESRF and the Spring-8. Temperature stability is the key factor in temperature scanning for high energy resolution. The fundamental difference between an analyzer and a normal-incidence, back-scattering monochromator is the surface area over which the temperature stability has to be maintained. In case of analyzers or highly asymmetric back-scattering monochromators, the area is much bigger than that of a normal-incidence monochromator so the temperature uniformity is as important as stability.

In order to keep temperature of the crystal uniform and under control a heat-exchange chamber is designed (figure, engineering drawings) The analyzer is located in the chamber and the chamber is then sealed with low temperature solder for low temperature measurements and a Teflon O-ring for high-temperature measurements. The heat-exchange chamber is filled with air, which is crucial for heat conductivity across the surface of the analyzer. In order to measure the temperature at two different points on the surface platinum resistors (PT 100) are used. The whole chamber is then placed in a vacuum environment, either an oven or a cryostat. The oven has the temperature range between ~ 295 K and ~ 475 K, which is defined by the glass transition temperature of the glue used to mount the windows on. On the other hand the He-flow cryostat can operate between ~ 40 K and ~ 350 K. Although the cryostat is capable of going down to 4 K, it was not possible to go below 40 K due to the heavy load.

Table 2.1: Potential use of sapphire analyzers for various transition metal K edges

Transition Metal	Incident Energy for RIXS (eV)	Miller Indices for Sapphire	Energy Resolution (meV)	Angular Acceptance (μrad)	Energy Tunability ^a (eV)
Fe	7130	(0 4 8)	32.0	3430	7115 - 7137
Ni	8340	(3 3 6)	9.5	1700	8311 - 8338
Cu	8990	(0 4 14)	16.9	1800	8981 - 8997
Zn	9680	(0 1 20)	23.0	1800	9648 - 9671

^aFor the temperature range between 50 K and 400 K.

2.3 Analyzer Design

2.3.1 Crystal Selection

The commonly used materials for high resolution analyzers, silicon and germanium have a single type of atom in a cubic unit cell (Figure 2.11). As a possible alternative, Al_2O_3 has a hexagonal unit cell with two different types of atoms (Figure 2.12). For Si and Ge, permutations of lattice indices would give the same plane due to the cubic symmetry of the structure. On the other hand, each permutation is a completely distinct case for sapphire since all the lattice parameters are different. Moreover, sapphire has two different kind of atoms (Al and O) in its unit cell, which means different atomic form factors function in the dynamical diffraction process. Thus, the selection rules for having an allowed reflection are much more relaxed compared to one-atom-unit-cells as in the case of Si and Ge. This less symmetric, multiple atom arrangement yields more than an order of magnitude more possible back-scattering planes to match with unique energies to be studied [41, 40] (Figure 2.13). Serendipitously, Al_2O_3 (0 4 14) has a 8991-eV back-reflection energy at room temperature with 84.5% theoretical reflectivity, which is a very good match for Cu K_{α} edge resonant inelastic x-ray scattering (RIXS) measurements. Possible sapphire planes for different transition metal oxide cases are summarized in the table ([50])

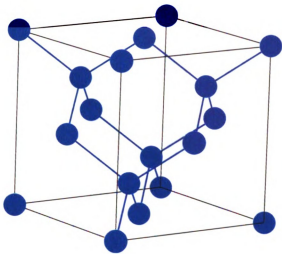


Figure 2.11: Silicon and germanium share the same simple cubic diamond structure with lattice parameters 5.431 Å [4] and 5.658 Å [5], respectively.

As the back-scattering energy is already very close to the energy at which RIXS measurements are performed, the analyzer can be designed to take advantage of this near back-scattering condition. Our analyzer operates at an 89.87° Bragg angle. The angular acceptance for Al_2O_3 (0 4 14) lattice reflection is then $1800 \mu\text{rad}$. This allows us to make 1.8-mm pixels along the scattering plane for a quasi-back-scattering analyzer located 1 m away from the scattering center without any loss of the intrinsic features of the crystal.

2.3.2 Cutting, Dicing, and Etching

Sapphire is a very hard material, and is ranked second in Mohs scale of mineral hardness after diamond (Table 2.2). This is a relative scale first established by the German mineralogist Frederich Mohs (1773-1839), who had sorted the known minerals, the hardest one being number 10 and the softest one, Talcum powder, being number 1. The hardness of a mineral can be determined by a simple procedure. The location

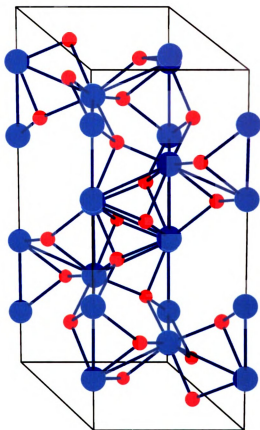


Figure 2.12: Sapphire has a hexagonal unit cell (R3c) with lattice parameters $a = b = 4.759 \text{ \AA}$ and $c = 12.991 \text{ \AA}$ [6].

of an unknown material on this hardness scale is above the hardest mineral that it can scratch and below the one that it can be scratched with. For example, a finger nail can scratch a gypsum but cannot scratch calcite, thus it has hardness of 2.5. A similar procedure has been also used to create a quantitative hardness scale by measuring the size of a standard indenter [51].

There are numerous ways to measure absolute hardness. One of the most used techniques is suggested by F. Knoop in 1939 [52]. To test the material, a pyramid shaped diamond is pressed against it for a period of time. The amount of load required to

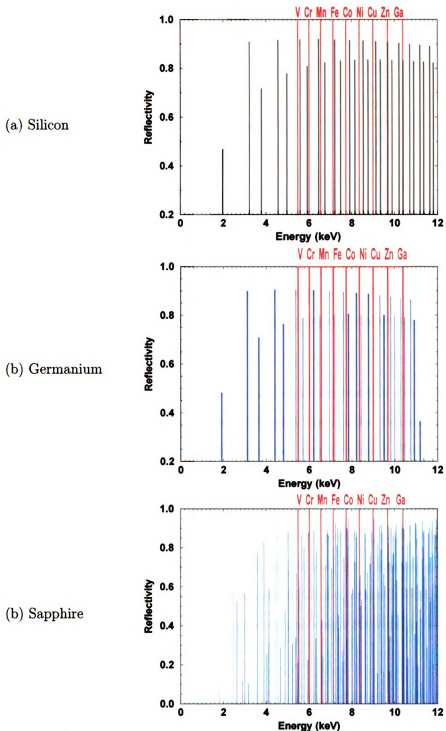


Figure 2.13: Back-scattering parameters are calculated according to dynamical theory of diffraction at 300 K. Red lines indicate the K-edge energies of the transition metal oxides. Blue lines are the unique back-reflections with their height showing the reflectivity. Sapphire, clearly, has much more distinct back-reflecting planes compared to Si and Ge.

Table 2.2: Mohs Hardness Scale

<i>Hardness</i>	<i>Mineral</i>	<i>AbsoluteHardness</i>
10	Diamond C	1500
9	Sapphire Al_2O_3	400
8	Topaz $Al_2SiO_4(F, OH)_2$	200
7	Quartz SiO_2	100
6	Orthoclase Feldspar $KAlSi_3O_8$	72
5	Apatite $Ca_5(PO_4)_3(OH, Cl, F)$	48
4	Fluorite CaF_2	21
3	Calcite $CaCO_3$	9
2	Gypsum $CaSO_4 \cdot H_2O$	3
1	Talc $(Mg_3Si_4O_{10}(OH)_2)$	1

make a unit area of indentation mark on the material is the Knoop Hardness number. In this absolute scale sapphire is ~ 3 times harder than quartz and ~ 7 times harder than silicon and germanium. Working with a hard material makes it challenging to fabricate instruments out of it.

Cutting is simply removing some of the materials from the body in a controlled way. It requires a harder material to penetrate and break the bonds. Wheels and blades with diamond grains are used to cut, polish, and dice sapphire pieces. Diamond grains are either embedded in a softer media or bonded on a metal surface. Metal bonded blades are not suitable for dicing hard materials like sapphire. Diamond grains should be bonded to the blade rather loosely, since in case it could not cut it should just pass without cutting and the next grain would do the job. If a diamond grain is not sharp enough it should just fall off. Metal bonded blades brake in such a case or apply more pressure than required. This pressure may cause fracture in the sapphire with the stress built up during cutting.

Another important factor is the grain size; smaller grains will just polish the surface instead of penetrating and cutting. A grain size in the order of 50 microns gave the best results. It is difficult to pack bigger grains in a small area that's why it is not easy to cut grooves on sapphire narrower than 200 microns. The key parameter in

dicing is the contact area per unit time. This defines the speed and diameter of the diamond wheel. For blades with 4.6" O.D.⁴ 200 micron thickness would give a surface area of 147 mm^2 . With these parameters 9000 rpm gave the best result. This means 22000 mm^2 area needs to be swept at every second. Test with different sizes of blades confirmed this number. The thickness and the rpm of the blade should be determined accordingly.

Groove depth is also important. Since sapphire is hard it is not recommended to cut it all at once. In order to cut a millimeter deep grooves one has to do multiple passes. Up to 250 micron deep is possible with a travel speed of 0.15 mm/s . However it is safer to cut only 100 micron during each pass. This number defines the travel speed (how fast the blade should move over the crystal). In order to cut deeper the blade should move slower keeping the amount of material to be removed per unit time constant.⁵

Grinding and cutting of the Al_2O_3 crystal introduces surface damage. These damaged layers are removed with an etchant composed of a 1:1 mixture of 95% sulfuric acid (H_2SO_4) and 85% phosphoric acid (H_3PO_4) at 300°C [53]. Removal rate depends on the temperature exponentially. It also is very much anisotropic that the ratio of etching rate for two different directions can be as high as 36. Relative composition of the ingredients can change the removal rate and anisotropy. Although annealing the sapphire pieces before etching is recommended in the literature, no effect was observed.

⁴Outer diameter.

⁵A simple arithmetic shows that dicing 1.5 mm pixels on a 2" diameter, 2 mm thick analyzer takes at least 27 hours with realigning the machine every one hour and a half.

2.3.3 Bonding Sapphire Wafers

The analyzer needs a special bonding technique that can tolerate the concentrated acids at the high temperatures involved in the etching process. The technique used here is the metallic diffusion bonding, which involves two layers of metal, i.e., Cu and Au, pressed against each other in vacuum at a temperature close to their melting point [54, 55].

A quick procedure to bond sapphire wafers can be summarized as follows. The surfaces to be bonded should be polished to a roughness better than a fraction of a micron and a flatness of a micron over the entire surface. The polished surfaces are separately coated with copper and gold layers with thicknesses of 400 *nm* and 1200 *nm*, respectively. Gold and copper surfaces are pressed against each other in vacuum at high enough temperature to allow metals to diffuse into each other, typically 900° for around half an hour. The higher the pressure is the better the diffusion will be. A pressure around 100 *kPa* at temperature as high as the melting point of one of the metals is recommended. The diffusion rate increases exponentially with increasing temperature.

Another method to bond sapphire is the spin-on glass bonding technique [56]. One or both surfaces to be bonded are coated with *SilicaFilmTM* and put together under a dead weight of couple of hundred grams. This sandwich is baked in a conventional furnace at 1600 Celsius for 4 hours. The Silica layer between sapphire wafers forms a metastable layer and creates a very strong bond between the two pieces. The biggest challenge here is achieving flatness better than a micron over the surface, which is not easy to obtain. Due to the poor flatness, the spin-on bonding did not work for these large-area sapphire wafers.

2.3.4 Step by Step

Here is a brief summary of the steps for preparing the sapphire analyzer. Sapphire wafers are etched for four hours initially. Grooves 1 mm deep and 200 μm wide are made on one side of a 1.5-mm-thick sapphire disk with surface normal oriented along the (0 4 14) lattice direction. After bonding this side to another flat sapphire wafer (300 μm thick) with an orientation different than the previous one, the remaining grooves are cut, leaving isolated pixels bonded to the sapphire supporting wafer. This two-sided cutting technique is to prevent scratching the supporting wafer, because any possible scratch may cause the wafer to crack during bending. After this last cutting step, the analyzer is etched for approximately 20 minutes. The whole assembly is then glued with epoxy resin (EPO-TEK[®] 301-2) to a blank concave sapphire lens with 1 m radius. Using the same material for the lens, substrate, and pixels helps prevent possible stress due to different thermal expansion coefficients.

Chapter 3

Performance Assessment of the Spectrometer: Be Phonons

In order to demonstrate the performance of the instrument, phonon excitations in beryllium were measured. The reason for this choice is the known dynamical structure of the crystal and its high counting rates.

Experiments were carried out at beam-lines 3-ID and 30-ID of the Advanced Photon Source. Synchrotron radiation was first filtered by a diamond (1 1 1) pre-monochromator to a level of 600 *meV*, then further monochromatized by a four-reflection Si (4 4 4) high-resolution monochromator to 22 *meV*. Monochromatic beam was scattered from a Be sample and analyzed by the Al_2O_3 (0 4 14) analyzer placed at an angle that defines the momentum transfer. The analyzed beam is focused back to the detector. The analyzer was 20 mm in diameter and placed 1 m away from the sample point. This geometry gives a solid angle approximately 3.24×10^{-4} steradians which determines the momentum resolution to be 0.16 \AA^{-1} .

3.1 Characteristics of the Analyzer

3.1.1 Resolution Measurements

As it is mentioned in Chapter 2, energy scanning can be performed by either keeping the incident energy fixed and varying the analyzer energy or vice versa. The analyzer energy can be scanned by either changing the Bragg angle or the d-spacing by varying the temperature. Figure 3.1 shows the spectrometer resolution curve measured by scanning the incident energy as well as measured by scanning the temperature of the analyzer when the incident beam energy was fixed. They are identical within experimental error, and the overall resolution is measured to be 38 *meV*. The reason to consider temperature scanning is not to lose the geometrical advantages by scanning the angle as explained in chapter 2.

Since the pixel size is smaller than the intrinsic angular acceptance of the Al_2O_3 (0 4 14) back-reflection, the only dominant geometrical contribution to the energy resolution is due to demagnification. According to section 2.2.2 and the equations therein, the expected contribution to the bandwidth due to demagnification is ~ 26 *meV*. This number depends on the size of the analyzer, the distance of the analyzer to the scattering center and to the detector, and the vertical off-set of the detector from the scattering center. Convolution of this geometrical contribution (ΔE_{geo}) with the intrinsic resolution of the back-reflection (ΔE_{cry}) and the incident photon energy bandwidth (ΔE_{mono}) gives the theoretically expected overall resolution of the spectrometer.

$$\Delta E = \sqrt{(\Delta E_{geo})^2 + (\Delta E_{cry})^2 + (\Delta E_{mono})^2} \quad (3.1)$$

For ΔE_{geo} of 26 *meV*, ΔE_{cry} of 17 *meV*, and ΔE_{mono} of 22 *meV*, the overall expected

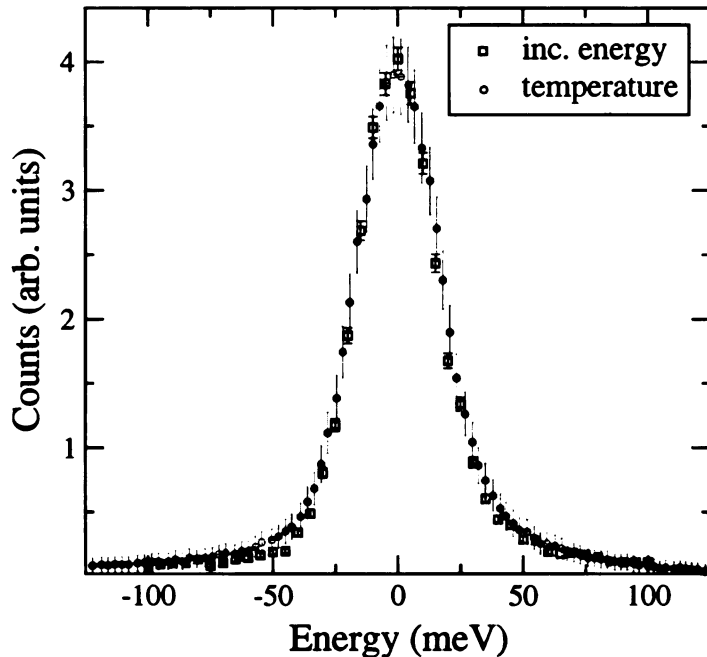


Figure 3.1: Overall instrumental resolution functions measured by two different scanning techniques. Open squares show the data taken by scanning the incident energy when the analyzer energy is kept constant. Open circles represent the data for the case when the incident energy is constant and analyzer temperature is scanned as a way of energy scanning.

resolution is calculated to be 38 meV, which agrees with the measurements.

The best fit to the line shape was obtained by using pseudo-Voigt function, which is a weighted linear combination of a Gaussian and a Lorentzian (see Figure 3.2);

$$w \frac{2A}{\Gamma \sqrt{\pi \ln 2}} e^{-\ln 16 \left(\frac{x-x_0}{\Gamma}\right)^2} + (1-w) \frac{2A\Gamma/\pi}{4(x-x_0)^2 + \Gamma^2} \quad (3.2)$$

where the first term is the Gaussian and the second term is the Lorentzian functions with weight factor w , which can take values between 0 and 1. A is the amplitude, x_0 is the point where the function takes its maximum, and Γ is the full width at half maximum (FWHM).

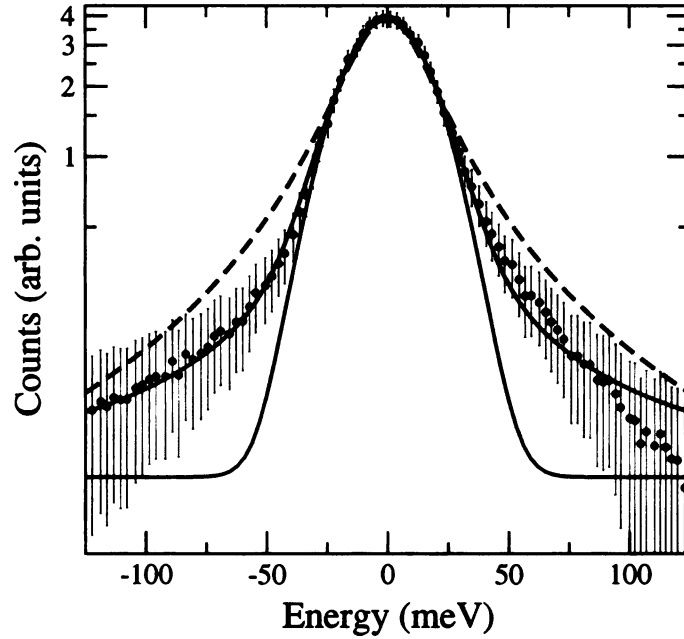


Figure 3.2: The fit function (blue) is a pseudo-Voigt function, which is a linear combination of a Lorentzian and a Gaussian. The solid and dashed lines show the normalized Lorentzian and Gaussian component of the fit, respectively. Y-axis is in log scale to see the tails better.

3.1.2 Energy Scanning and Calibration of the Instrument

The average thermal expansion coefficient of sapphire is $5.35 \times 10^{-6} K^{-1}$ at room temperature (see Figure 3.3) [57]. Back-scattering energies for the Al_2O_3 (0 4 14) lattice reflection at 100 K and 500 K are 9001.0 eV and 8977.61 eV, respectively, which gives more than 20-eV scanning range. The requirements for the temperature scanning is chapter 2¹.

The energy bandwidth broadening due to the uncertainty in temperature of the crystal can be written with reference to Eqn. 2.20;

¹The pictures of the oven and the cryostat together with the heat exchange chamber are given in the appendix with detailed explanations.

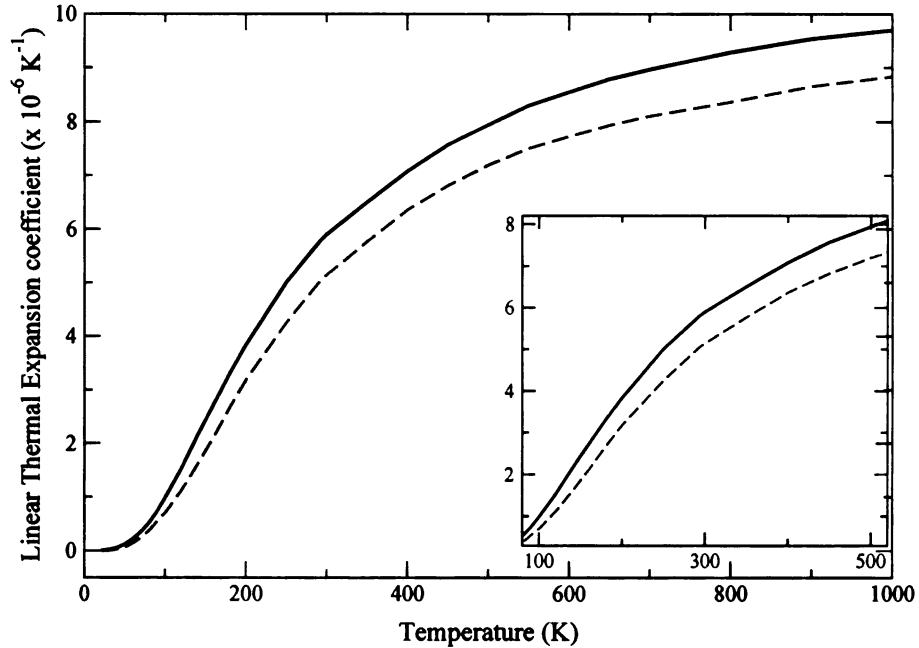


Figure 3.3: Linear thermal expansion coefficient of sapphire for the direction parallel to c -axis (solid black) and for the direction perpendicular to c -axis (dashed red). At temperatures below 100 K , it approaches to zero and further cooling does not change the lattice parameters much. The inset has the portion accessible with the current instrumental limits.

$$\frac{\delta E}{E} = \alpha \delta T \quad (3.3)$$

where α is the linear thermal expansion coefficient (LTEC) and δT is the uncertainty in temperature. LTEC is approximately $5.43 \times 10^{-6} K^{-1}$ perpendicular to sapphire (0 4 14) plane. This corresponds to $\sim 48.8 meV$ energy change for 1 K of temperature variation for photons at energies in the order of 9000 eV . For a resolution of 38 meV , temperature variations around 50 mK or better has virtually no effect. The achieved temperature control during the experiments provided stability in the order of mK .

Temperature scans take longer than (mechanical) angular scans. The response of the system is very slow and gets slower with increasing mass load. Stabilizing the

temperature takes at least half an hour with the current setup. Therefore it is not practical to change the temperature and wait as a way to do the measurements. Instead, the measurements should be taken on a sweep.

Here is a good procedure to perform temperature scanning:

1. Decide what is the starting energy and calculate the approximate temperature
2. Go a few hundred meV below (assuming the scanning is from a lower end of the range to the higher energies), a few hundred meV corresponds to $\sim 10 K$. Let the temperature stabilize (this step may take longer as it requires to set-up a PID module²)
3. Decide the counting time, based on how good the statistics should be
4. During the counting time the temperature should not change more than $50 mK$, which corresponds to $\sim 3 meV$ that is tolerable for a $38 meV$ -instrument. For higher resolution measurements, the scan rate has to be slower. Calculate the temperature steps accordingly.
5. Decide up to what energy (temperature) the scan should be performed.
6. Calculate the number of steps, which is initial temperature subtracted from final temperature, divided by the step size that is determined at step 4.
7. To start the temperature ramp up, add at least $1 K$ to the set temperature of the PID module. This would give an initial kick as the response of the system is slow.
8. Set up a scanning module (a small software or do it by hand) that periodically adds an amount, which has been decided at step 4, to the set temperature in the PID module.

²More information on PID temperature control can be found at http://www.lakeshore.com/pdf_files/Appendices/LSTC_appendixF1.pdf

9. Make a dry run just to see how the temperature rises, note that the readings from resistors or thermocouples should be recorded, and not the set temperatures of the PID unit.
10. Tweak the parameters to a satisfactory level. Make sure the starting temperature is the same every time and enough time is given to the system so that it stabilizes.
11. Do a second dry run to calibrate the energy. Detail will be given in the following section.
12. Without changing the parameters (starting temperature, step size and waiting time) start the scan. If for any reason the scan has to be aborted, go to the starting temperature and start from the beginning. No pausing works for this procedure.

Energy Calibration

Energy has to be calibrated for two reasons. First of all temperature readings cannot be absolute to the point that allows us to use the theoretical values for both the d-spacing and the energy. Besides, temperatures are measured on two different points of the analyzer. Even if the readings are absolute, the readings will be different, it requires a detailed analysis to decide what temperature to be used.

To calibrate the energy, the dry run has to be performed with an elastic scatterer as a sample. While the temperature is ramping up a quick incident energy scanning will result a peak centered at the incident energy when it matches the analyzer energy. This gives the energy value corresponding to the average analyzer temperature during the scan. These values should be recorded. By just repeating the process over and over a table or a graph of calibration can be obtained. Figure 3.1.2 shows a graph

obtained as a result of such a dry run for calibration. Vertical axes are the angles of the monochromators which can be converted to energy easily. Remember energy is now scanned by changing the incident energy via angular scans of the monochromator crystals. The flat looking pieces are actually the individual scans (Figure 3.1.2).

Temperature scanning yields a data that is composed of temperature and the photon counts. The temperature field should be replaced by the energy with reference to this calibration.

Note that the calibration is specific to particular scanning parameters since at different temperatures none of them including the thermal expansion coefficient and ramping rate are constant. They may be similar for different cases, but scanning without calibration would result in more error that has to be taken into account during the analysis of the data.

3.2 Sample and the Sample Environment

The beryllium crystal used in this experiment is the original crystal used by E. Burkel twenty years ago to measure the phonon excitations with IXS for the first time [23]. Be has a hexagonal closed-pack (hcp) crystal structure with lattice parameters $a = 2.2858 \text{ \AA}$ and $c = 3.5843 \text{ \AA}$. The phonon intensities are measured along $[00\zeta]$ direction at the first and second Brillouin zones.

For inelastic x-ray scattering measurements the elastic signal should be eliminated as much as possible. For times when the elastic signal is non-existing, in order to have a reference to measure energy transfer, a little elastic signal may be required. Other than that elastic peak usually degrades the quality of the spectra. The major contributor to elastic signal is the imperfections or impurities in the sample crystal. It is essential to have a good-quality sample however most interesting samples cannot

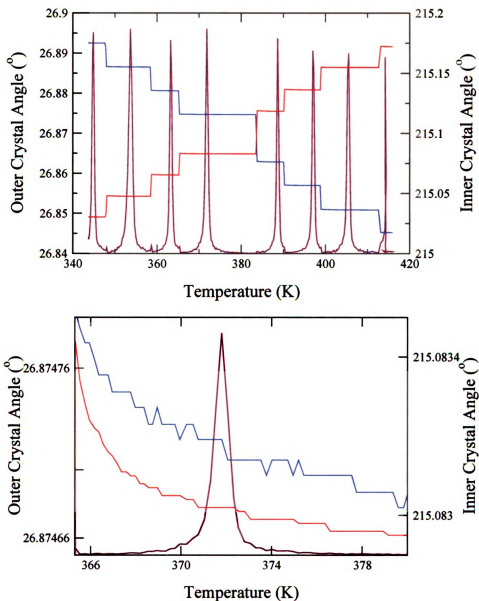


Figure 3.4: On the top graph, every single peak corresponds to an individual energy scan that is performed by changing the incident energy. Incident energy can be calculated precisely as the goniometers used are connected to encoders with 10^{-5}° precision, which gives an accuracy of $\sim 0.5 \mu\text{eV}$ in energy for the current setting. Since the energy scans are much faster than the energy change due to the temperature variation, the uncertainty involved here can be neglected. The blue (red) curve shows the angle of the outer (inner) pair of the monochromator crystals. In the zoomed view, both angles are scanned in the same direction. The only reason is to avoid the backlash of the scanning motors. This should not cause any confusion.

be grown very big. A practical way to go around this problem is focusing the beam to reduce the footprint on the sample. Thus very small samples or perfect but small piece of a big mosaic sample can be measured. Alignment can be more challenging in these cases.

Even for perfect crystals elastic signal may come from the sample surface or the sample environment. A polished, good-quality, and clean surface is recommended to avoid the elastic signal due to the surface effects or dirt on the surface. Sample should be placed in vacuum in order to eliminate the elastic signal from air in the close vicinity of the sample.

At the time of measurements, due to some technical problems, the beryllium crystal was not put in vacuum. Most of the noise in the data is due to the elastic scattering from the air.

3.3 Detector

Detector is another essential part of an inelastic x-ray spectrometer. Since the inelastic signal is already low and the photon count at an inelastic peak can be as low as one photon per minute, the detector should have virtually zero dark count. The dark count can be defined as the average number of photons detected without any source. It can originate from the heat as well as the electronics.

The detectors used in our spectrometer are solid state diodes by Amptek[®]. Cd-Zn-Te diodes are suitable for relatively higher energies compared to Si diodes due to their higher absorption. More important point for a detector for these low signal instruments is the detector housing. As in Figure 3.5 the incident beam is very close to the detector chip as it is crucial for being close to back-scattering. The incident beam here means the beam scattered from the sample that is incident on the

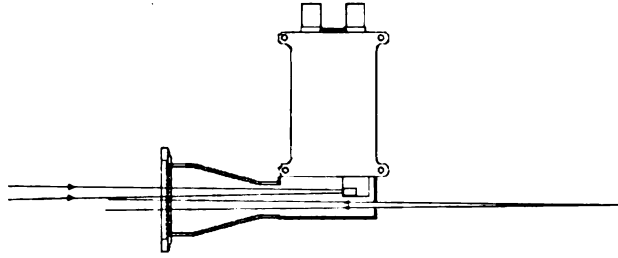


Figure 3.5: Detector from the side view. Spherically scattered beam (red) from the sample is focused (blue) on the detector chip after back-reflection from the analyzer. Detector housing material should be chosen so that the fluorescence radiation energy can be discriminated from the primary signal energy with detector's resolving power. Aluminum is a good choice for copper edge experiments.

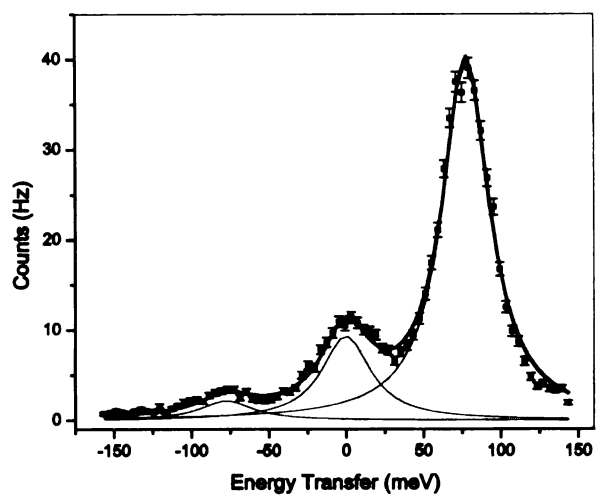
analyzer, not the beam incident on the sample. The beam scattered from the sample has photons of both elastic and inelastic origin over a solid angle of 4π . Only a very small fraction of this beam will satisfy the Bragg condition on the analyzer and be focused to the detector. On the way to analyzer the scattered beam hits the detector housing. Elastic scattering from the housing material as well as the characteristic emission lines from the elements in the housing might go to the detector chip and contaminate the signal. Specially for relatively low energy measurements like copper K-edge RIXS, a steel housing that contains Fe, Ni, and Cr gives emission lines that are close in energy to the copper K-edge energy and not easily discriminated. Instead, an aluminum housing is preferred and the background improved drastically.

3.4 Results

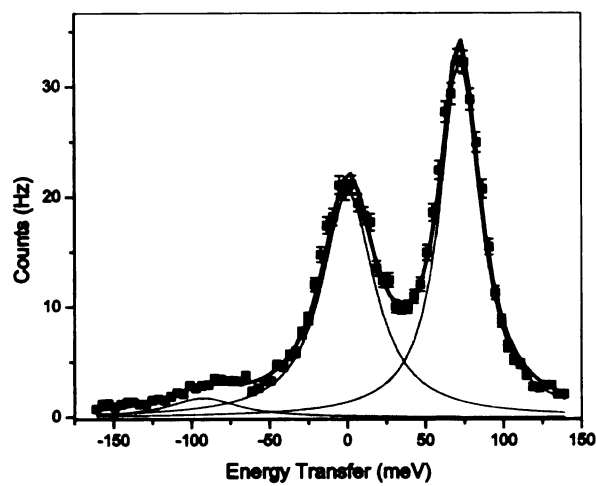
Since there is no resonance effect expected around 9000 eV for Be measurements, spectra were collected by scanning the incident energy. Phonon excitations at energies as low as 28 meV were observable as a demonstration of the resolving power of the spectrometer (see Figure 3.6). Spectra can be best fitted by employing pseudo-Voigt

function, which is a linear combination of a Gaussian and a Lorentzian with variable weight parameters (see section 3.1.1). This is because the peaks are composed of the the resolution function of the crystal optics, delta-function-like phonons, and random Gaussian distribution as it is the case in any measurement. Resolution function of the crystal optics can be best approximated as the Lorentzian line shape due to fast drop of the peaks with high tails on the sides. Figure 3.7 shows the dispersion of the phonon peaks compared with data taken previously [7, 8].

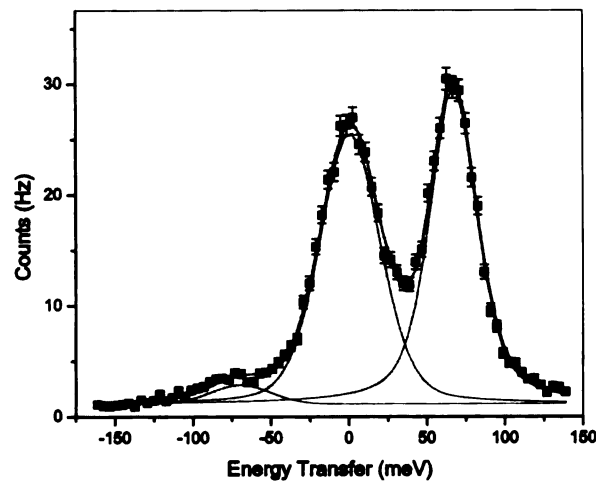
$\zeta = 0.8$



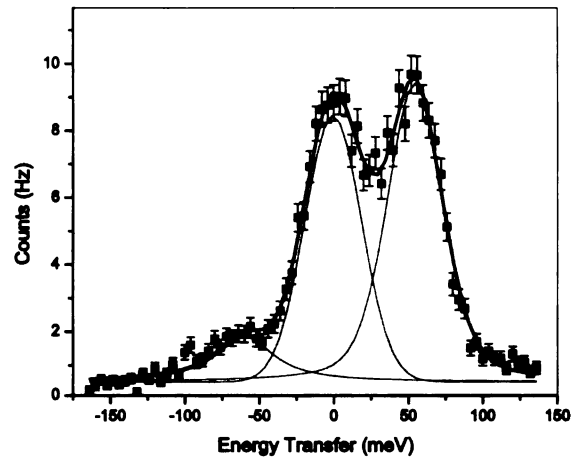
$\zeta = 0.7$



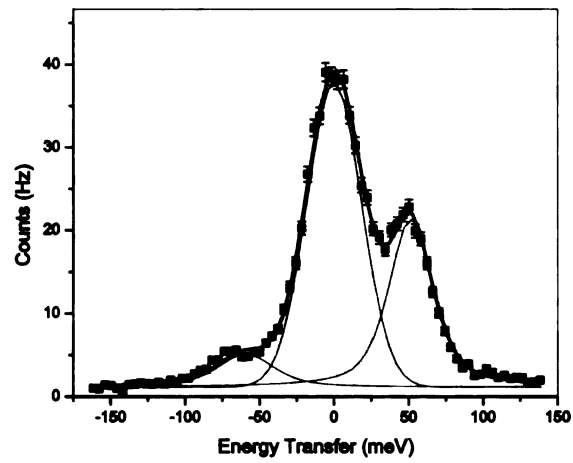
$\zeta = 0.6$



$\zeta = 0.5$



$\zeta = 0.4$



$\zeta = 0.3$

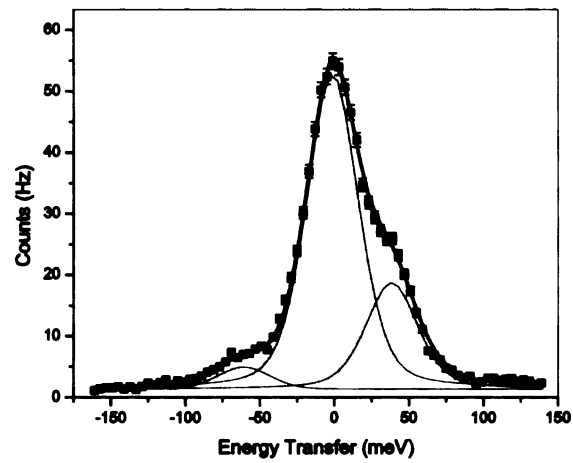


Figure 3.6: Individual spectra measured at six different momentum transfer values defined by $\zeta \frac{2\pi}{c}$.

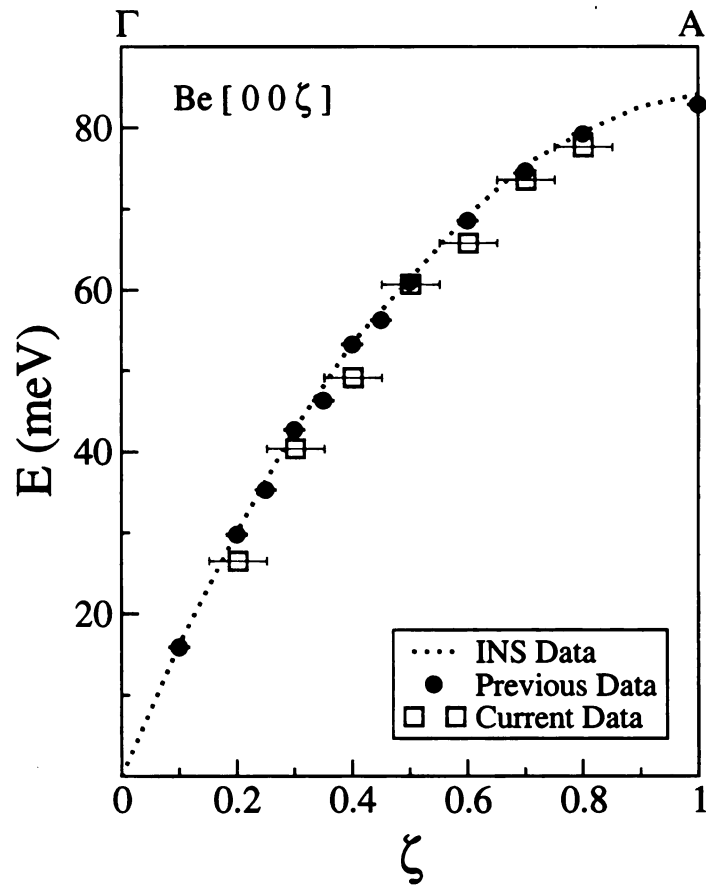


Figure 3.7: Be phonon dispersion measured along the $(0\ 0\ \zeta)$ direction, where momentum transfer vector is along the c -axis with magnitude equal to $\zeta \frac{2\pi}{c}$. Measurements are compared to published data by Alatas [7] (solid black circles) and Stedman [8] (dashed line).

Chapter 4

RIXS Study on Phonons in CuO

4.1 Background and Motivation

The mechanism of superconductivity at high critical temperatures has not yet been resolved, in spite of many years of extensive research. One of the major causes behind this enigma is that many correlation effects take place in these materials and the interplay among them is not well understood. The fact that most, if not all, high T_c superconductors share the same CuO_2 plane directed a considerable amount of intellectual resources towards investigating cuprates. As the conventional approaches, including the *BCS theory*, fail to explain the exotic phenomena in these systems, many believe that the underlying causes of superconductivity in cuprates must be due to the strong correlation of electrons. Electronic and magnetic correlations cannot be excluded completely for cuprate super conductors. However there is strong evidences that coupling of electrons with the lattice might also be playing important role [58, 59, 60].

Sharing the same integral CuO_2 placket with the high T_c superconducting cuprates (HTSC) (Figure 4.1), CuO is of particular importance since it is the simplest member of this family. The crystal structure of CuO has monoclinic symmetry [36]. Every

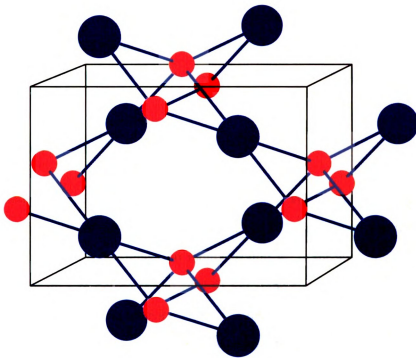


Figure 4.1: Monoclinic structure of CuO. Oxygen atoms (small red) around copper atoms (big blue) form a ribbon-like bands along $(1\ 1\ 0)$ and $(1\ -1\ 0)$.

copper is surrounded by four oxygen atoms forming a ribbon-like planes along $(1\ 1\ 0)$ and $(1\ -1\ 0)$ directions. These two bands intersects with an angle of about 78° , and the line of intersection is along $(0\ 0\ 1)$ direction. CuO is an anti-ferromagnetic semiconductor with an indirect gap of around $1.35\ eV$ [61].

The lattice dynamics of CuO has been studied by various techniques, including Raman [62, 63], infrared [64], and inelastic neutron scattering [65], showing signs of spin-phonon and charge-phonon coupling. In this dissertation, resonant inelastic x-ray scattering (RIXS) measurements of the lattice excitations as a function of momentum transfer is suggested as one more tool to reveal complementary information on the way to comprehend the nature of electron-phonon coupling in correlated electron systems. Although the mechanism and cross-section of RIXS are not precisely known, it is

believed that the strong core-hole potential, as a result of K-edge absorption, causes electronic excitations in the valence band [35, 3]. If the electronic excitations caused by this K-edge absorption are in the order of room temperature, it is evident that these low energy charge and spin excitations naturally couple with the lattice excitations.

4.2 Experimental Details

RIXS is employed for the first time to study the lattice vibrations. The X-ray beam from the undulator beam-line, 3-ID at the Advanced Photon Source, was first filtered by a diamond (1 1 1) double-reflection monochromator. A toroidal mirror was used to reduce the beam size before the Si (4 4 4) four-reflection monochromator, which is located 40 *m* far from the source. Using a mirror provides a smaller beam size, however locating it before the monochromator sacrifices the efficiency due to the reduced collimation. The number of photons on the sample was 1.7×10^{10} with spectral bandwidth of 22 *meV*.

Phonon excitations are not expected beyond 100 *meV*. This gives the flexibility to limit the energy scanning range to be maximum ± 200 *meV*. Resonant behavior, if there are any, are known to be wide enough to cover this range. Absorption parameters are also expected to remain almost constant. As a result, it would not hurt to do the energy scanning by changing the incident energy with fixed analyzer energy. During this present analysis, the incident energy will be considered to be fixed for each individual scan.

The CuO single crystal, with an approximate size of 45 *mm*³, was grown and oriented along (1 0 0) direction¹. The sample was in vacuum to reduce the background due to air scattering. Since there is evidence that the electron-lattice coupling is strongest at the zone boundary [59], the measurements were taken along (1 0 0) direction. The

¹Thanks to G. Behr, M.-O. Apostu, and N. Wizent, IFW, Dresden, Germany

electric field of the incident x-ray beam was along the (0 0 1) direction. This is a pure σ -polarization for both of the CuO_2 planes since the polarization of the incident light is oriented parallel to the intersection axis of these planes. Momentum transfer along (1 0 0) vector has components on both of the CuO_2 bands.

Newly developed Al_2O_3 (0 4 14) analyzer made these measurements possible with its high resolution at the copper K-edge energy [66]. The overall resolution of the spectrometer was 38 *meV*. Doing the measurements at the zone boundary was particularly suitable with this kind of resolution since the phonon branches disperse to their highest frequency at the zone boundary, which makes it easier to distinguish them from the elastic signal.

Measurements were taken at four different incident photon energies across the K-edge absorption of copper². The fluorescent spectrum (Figure 4.2) shows the incident photon energies and their relative location with respect to the absorption edge. All four values are between the quadrupole and dipole transition energies.

As a complementary test, non-resonant inelastic x-ray measurements were also done at the same geometry except the electric field vector of the incident photon beam was on the scattering plane (partial π -polarization)³. Data were collected along the (1 0 0) direction at six different momentum transfer points (Figure 4.3). The spectra are mostly in agreement with the inelastic neutron measurements [65]. Surprisingly, at the zone boundary ($\xi = 1.00$), where the resonant measurements were done, inelastic signal was almost non-existing.

²In order for the analyzer to perform at different energies, the analyzer temperature was changed and kept constant while the energy scanning was performed by changing the incident photon energy. For more details see Chapter 3.

³For the non-resonant measurements, the incident photon energy was 21 *keV* and the overall resolution of the spectrometer was ~ 2 *meV*.

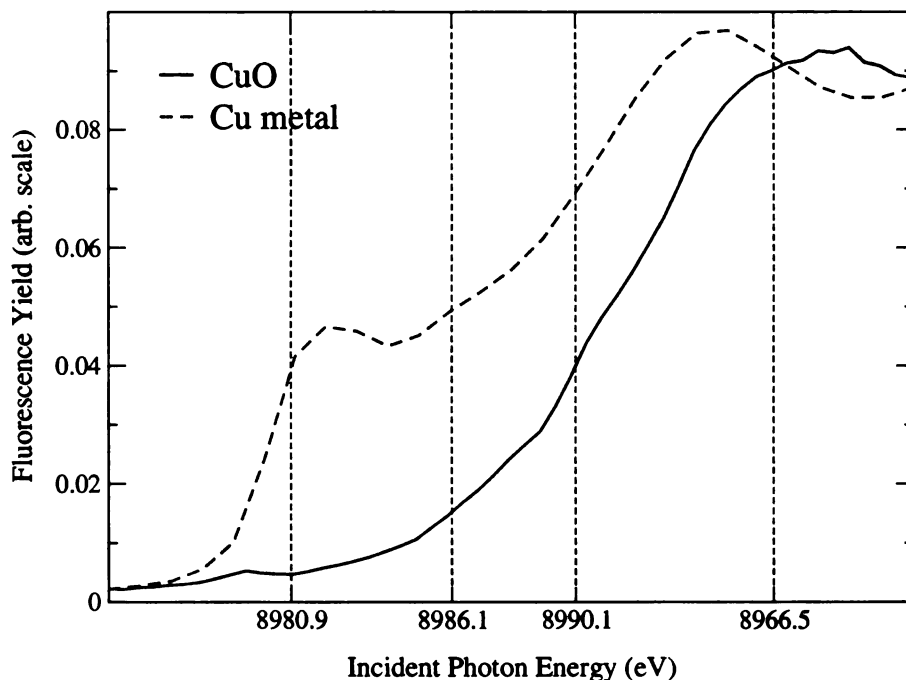
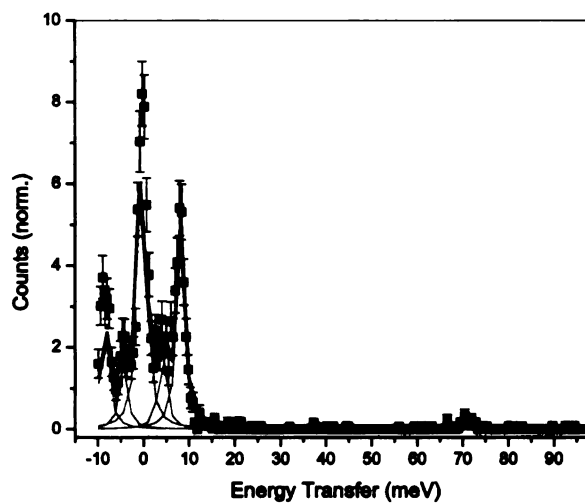


Figure 4.2: The red (dashed) line shows the fluorescence spectrum across the copper K-edge absorption while the blue (solid) line shows that of CuO crystal. The quadrupole and dipole transitions occur at about 8979.5 eV and 8998.5 eV, respectively. The dashed vertical lines indicates the incident photon energies at which the measurements were taken.

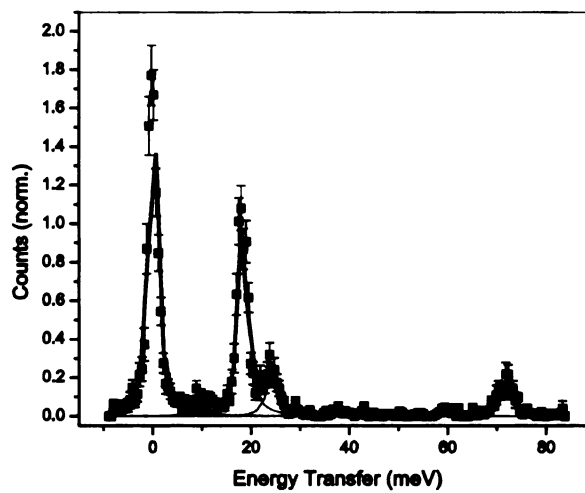
4.3 Discussion

These first of their kind measurements clearly show that phonon spectra measured by the inelastic x-ray scattering technique depends on the incident photon energy. The monotonic change in the spectra as a function of incident energy can be shown by fitting the individual spectrum with three Lorentzian functions; one being the elastic peak in the middle and two on each side indicating creation and annihilation of excitations (see Figure 4.3). The inelastic interaction of x-ray photons (or neutrons) with one phonon was believed to be represented by the dynamical structure factor [67] as

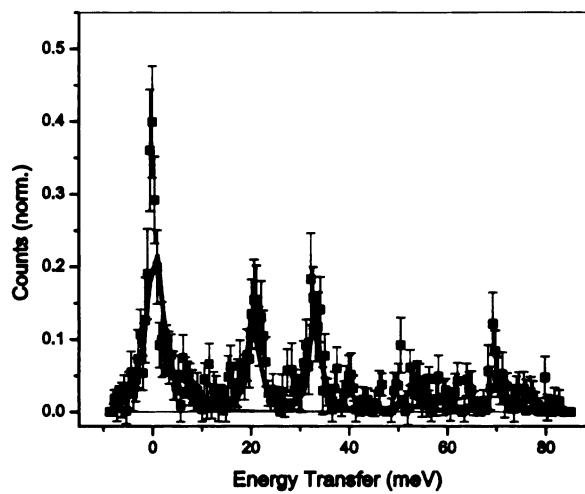
(a) $\xi = 1.85$



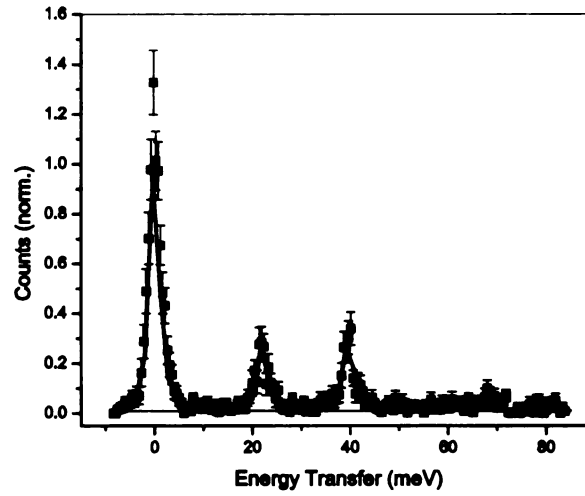
(b) $\xi = 1.60$



(c) $\xi = 1.35$



(d) $\xi = 1.10$



(e) $\xi = 1.00$

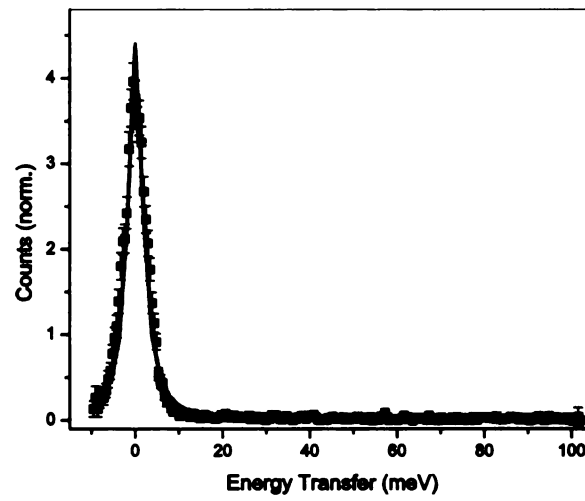


Figure 4.3: The non-resonant inelastic X-ray scattering measurements of CuO at six different momentum transfer point. Surprisingly, at the zone boundary, $\xi = 1.00$, where the RIXS measurements are done, no inelastic signal was detected.

$$S(\vec{Q}, \omega) = \frac{\hbar}{2M\omega_0} |\vec{Q} \cdot \vec{e}_{\vec{Q}}|^2 [(n+1)\delta(\omega - \omega_0) + n\delta(\omega + \omega_0)] e^{-2W(\vec{Q})} \quad (4.1)$$

where M is the mass of the vibrating atom, $\vec{e}_{\vec{Q}}$ is the phonon eigenvector which determines if the phonon is visible at a certain polarization, n is the occupation number of phonon, ω_0 is the phonon frequency, ω is the energy transfer to the phonon divided by \hbar , and the last term is the Debye-Waller factor.

The intensity of the measurements can be calculated by using the following double differential equation:

$$\frac{d^2\sigma}{d\Omega d\omega} = N \left(\frac{d\sigma}{d\Omega} \right) S(\vec{Q}, \omega) \quad (4.2)$$

where N is the number of atoms, $\left(\frac{d\sigma}{d\Omega} \right)$ is the Thompson scattering length, which is the square of the classical electron radius, r_0 . Clearly, there is no dependence on the incident photon frequency.

For photon energies much greater than an absorption edge of the atom or for neutrons⁴, there is no question about this representation (Eqns. 4.1-4.2) as it agrees with two decades of empirical research⁵. However, for the inelastic x-ray scattering measurements, when the incident photon energy is in the vicinity of the K-absorption-edge, either the theory fails or the lattice excitations couple with other low energy excitations that the current measurements are a demonstration of this effect.

The reason for this curious effect can be emergence of new phonon branches that are not visible otherwise. The dependence of the spectra on the incident energy together with the almost non-existing inelastic signal for the non-resonant IXS measurements seem to support this idea. However, the visibility of lattice excitations is known to depend on the overlap of the phonon polarization with the momentum transfer vector

⁴Neutrons do not couple with charge.

⁵For neutrons, it is more than half a century.

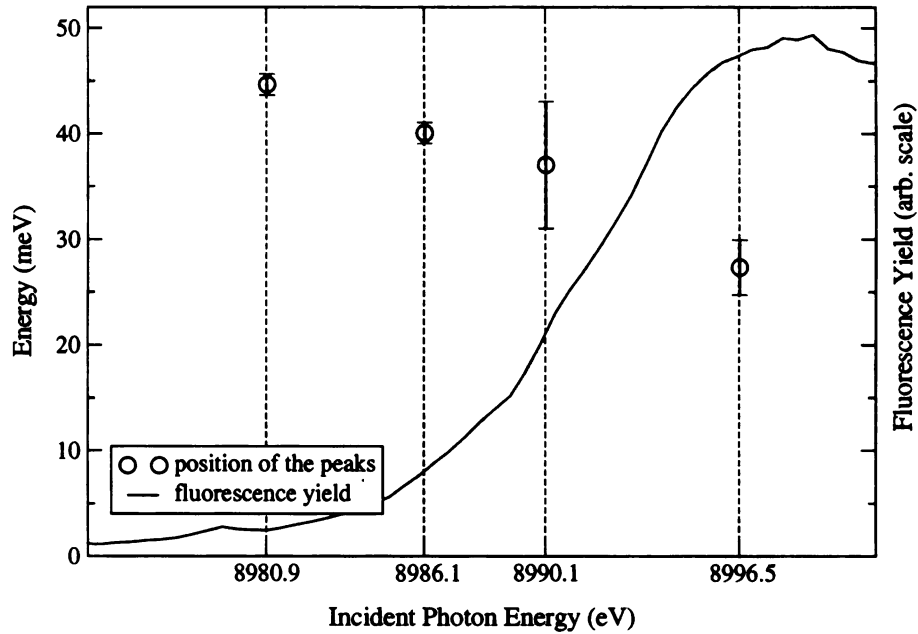


Figure 4.4: The open red circles with error bars show the center of mass of inelastic peaks that are obtained by fitting the spectra with three Lorentzian functions.

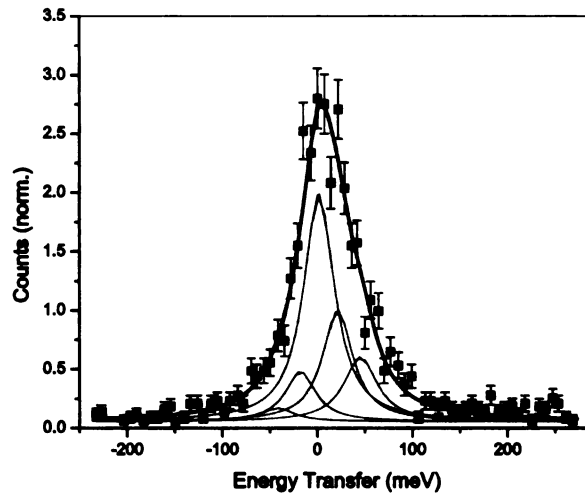
of the incident beam (see Eqn. 4.2). The quality of the data is far from sufficient to come to such a conclusion. Another possibility one might think of is the change in phonon frequencies. Phonon frequencies depend on the corresponding force constants between the atoms associated with the particular mode in question. A strong core-hole potential as a result of photon absorption during the RIXS measurements sure breaks the symmetry of the bonds, however the lifetime of the core hole is more than 2 orders of magnitude shorter than the phonon time scale. This mismatch assures that the possibility one exiting photon sees a modified phonon frequency should be excluded.

The INS measurements show that the phonon branches disperse towards the zone boundary and take their maximum frequency. In the vicinity of the zone boundary the dispersion slows down and becomes almost flat. The non-resonant IXS measurements at $\zeta = 1.10$ shows that there are two particularly pronounced phonon branches.

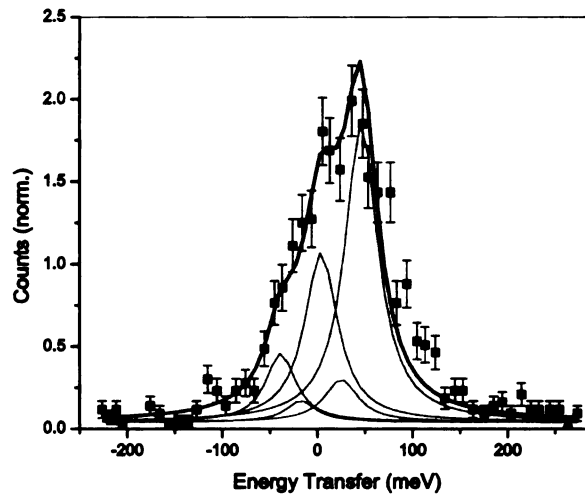
Assuming the same phonons are also detectable during the RIXS measurements, a fit attempt can be done by fixing the phonon energies and leaving the intensities as free parameters. By doing so, it is implicitly claimed that the relative intensities of phonon peaks in the spectrum changes while the frequencies remain the same. Figure 4.5 shows the individual RIXS scans fitted by five Lorentzian peaks. The middle peak is the elastic signal while the two on each side are the phonon peaks at ~ 20 meV and ~ 40 meV, and their energy gain side counterparts. The energy gain side peaks correspond to annihilation of phonons, the amplitudes of which are kept within detailed balance factor⁶.

⁶The probability of creating phonons is more than that of annihilating an existing phonon excitation by a factor $e^{\hbar\omega/kT}$, where ω is the phonon frequency, k is the Boltzmann constant, and T is the sample temperature.

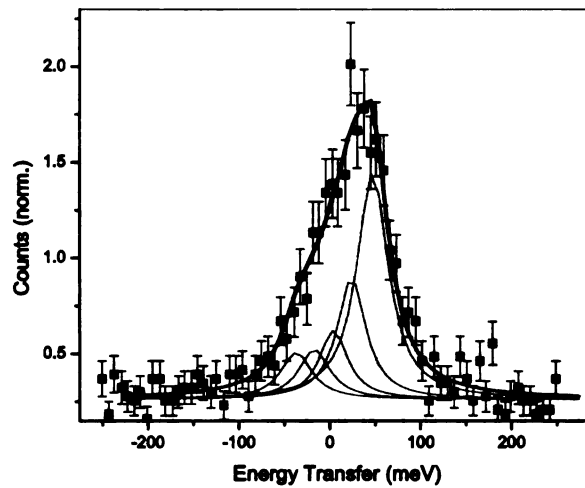
(a) $E_{inc} = 8996.5 \text{ eV}$



(b) $E_{inc} = 8990.1 \text{ eV}$



(c) $E_{inc} = 8986.1 \text{ eV}$



(d) $E_{inc} = 8990.9 \text{ eV}$

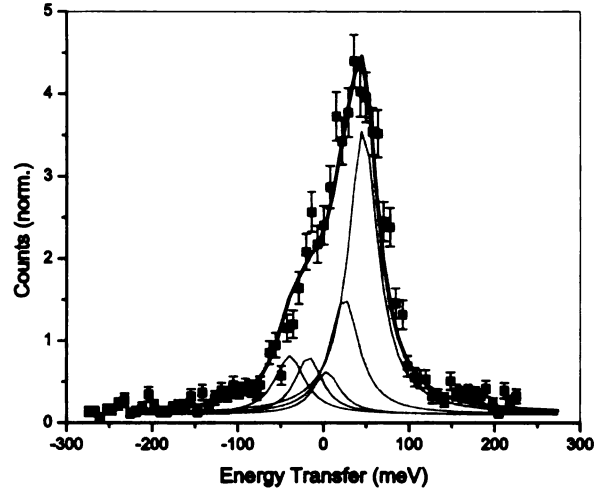


Figure 4.5: Individual scans of the RIXS measurements at the zone boundary, $\zeta = 1.0$. They are normalized with the incident number of photons. The y-scale has to be multiplied by 10^{-5} to get the cross-section per incident photon. The spectra are fitted by five Lorentzian peaks, the positions of the peaks are constrained so that the phonon peaks are at $\sim 20 \text{ meV}$ and $\sim 40 \text{ meV}$. The intensities are also constrained so that they obey the detailed balance factor.

The individual scans clearly contradict with the non-resonant measurements at the zone boundary. The width of the elastic peak for the non-resonant data is $\sim 3 \text{ meV}$, which is comparable to the spectrometer resolution. On the other hand, resonant data shows inelastic signal around the elastic peak. If one considers the data as a single peak, the full width at half maximum (FWHM) of the (the minimum is $\gtrsim 60 \text{ meV}$) appear to be greater than the spectrometer resolution of 38 meV .

Figure 4.3 shows the intensity ratio of the 40 meV -phonon intensity to the overall integrated intensity as well as the ratio of the elastic signal to overall integrated intensity. The latter shows a monotonic increase of elastic signal ratio which suggests an elastic decay channel that has yet to be discovered.

Near the quadrupole transition energy, where the core level electron is excited to copper $3d$, the ratio of the 40 meV -peak to the overall integrated intensity is maximum.

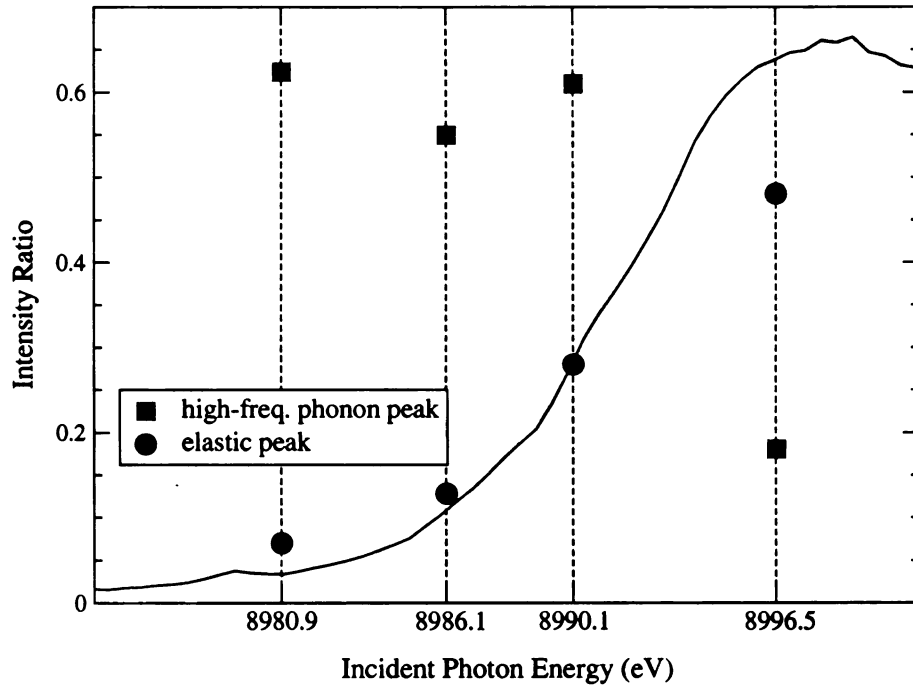


Figure 4.6: The red (square) symbols show how the ratio of the high-frequency phonon intensity to the overall integrated intensity changes as a function of incident energy. The blue (round) symbols show the change in the ratio of elastic signal to the overall integrated intensity.

This relatively higher energy phonon is attributed to $Cu - O$ stretching mode, which is expected to be changed as a result of this excitation. The reason is that the extra electron added to $3d$ level breaks the symmetry of the orbital. Again the time scale mismatch prevents this change from being observed.

Restricting the fit parameters to obey detailed balance ratio actually contradicts with suggesting intensity enhancement of certain phonon modes. This explanation claims that the number of phonons created are enhanced due to resonance, which does not include the existing phonons about to be annihilated. In order to check that, the measurements can be repeated with low sample temperature to suppress the phonons in the sample.

One more possibility is that the observed effect is not of phonon nature. It might

be a low energy charge excitation that is enhanced due to resonance. There is no known study on RIXS measurements estimating excitations in the order of room temperature. Therefore, while these observations can be stated precisely, ultimate theoretical implications have yet to be determined.

Chapter 5

CONCLUSION

A new high-resolution X-ray spectrometer was designed to study the low energy excitations in cuprates at the copper K-edge absorption energy. The new analyzer was fabricated, tested, and used to demonstrate its potential. It is shown that alternative crystals can be considered to meet specific requirements for RIXS measurements. For copper K_{α} edge experiments, the Al_2O_3 (0 4 14) lattice reflection appears to be a good match with regard to resolution, angular acceptance, and reflectivity. The novel feature of this spectrometer over other RIXS instruments is that the analyzer operates very close to back-scattering. This enhances efficiency without sacrificing resolution. As an example, Be phonon dispersion has been measured and compared with data reported by others [7, 8]. It may be possible to further improve collection capacity by making larger analyzers.

To demonstrate the possible benefits of using such a spectrometer, low energy excitations in cupric oxide was measured as a function of incident photon energy. The overall spectral resolution of 38 meV was not enough to resolve the individual peaks, however it is possible to see the changes. The change in the spectra could be due to a resonance effect on phonons or some low-energy electronic excitations that could not be realized earlier. There is no unique fit to the data however with some restrictions,

some predictions could be made about the nature of the excitations.

5.1 Future Outlook

The measurements should be repeated with better statistics and greater resolution. The intrinsic resolution of sapphire (0 4 14) is 17 meV , which makes it possible to design a spectrometer with higher resolution provided that there are enough photons. A sensible test would be to repeat the measurements at low sample temperatures so that the energy gain side (annihilation of existing excitations) has virtually zero intensity. This would make the fitting easier and serves as a check for the phonon-enhancement scenario.

Appendix A

Instrument Parts

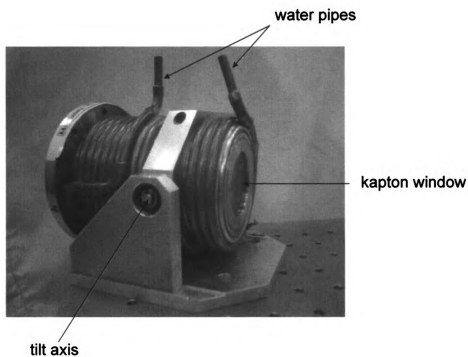


Figure A.1: Water lines are to cool the outer jacket of the oven for temperature stability. *Kapton*[®] polyimide film by *Dupont*TM is used for the front window. Two axis is enough to orient the crystal in the oven. Oven has a built in stage for horizontal axis rotation (tilt).

A.1 Engineering Drawings of the Heat Exchange Chamber

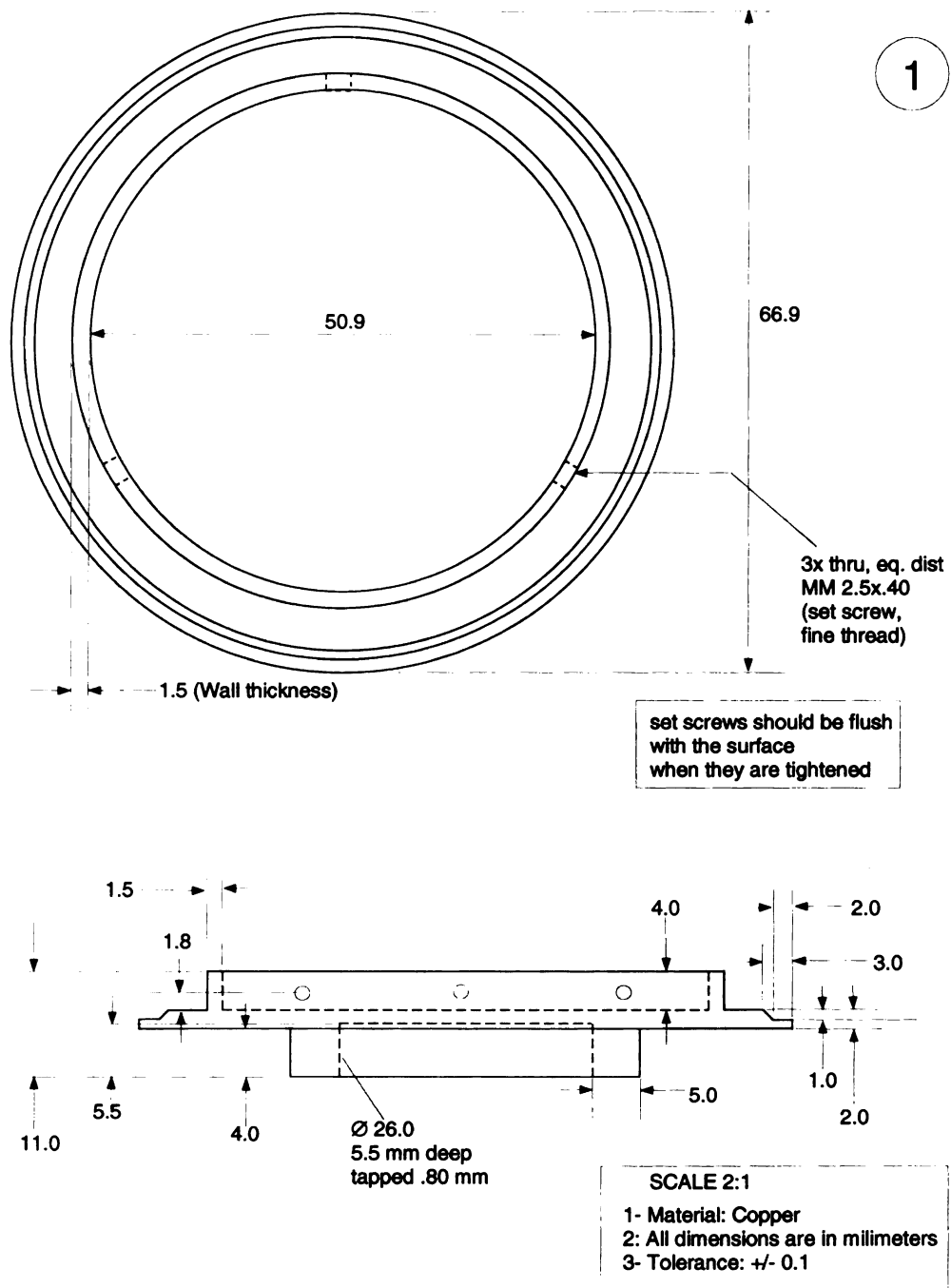


Figure A.2: Top and side view. This is the part where the analyzer is actually placed. Set screws are to fasten the analyzer substrate.

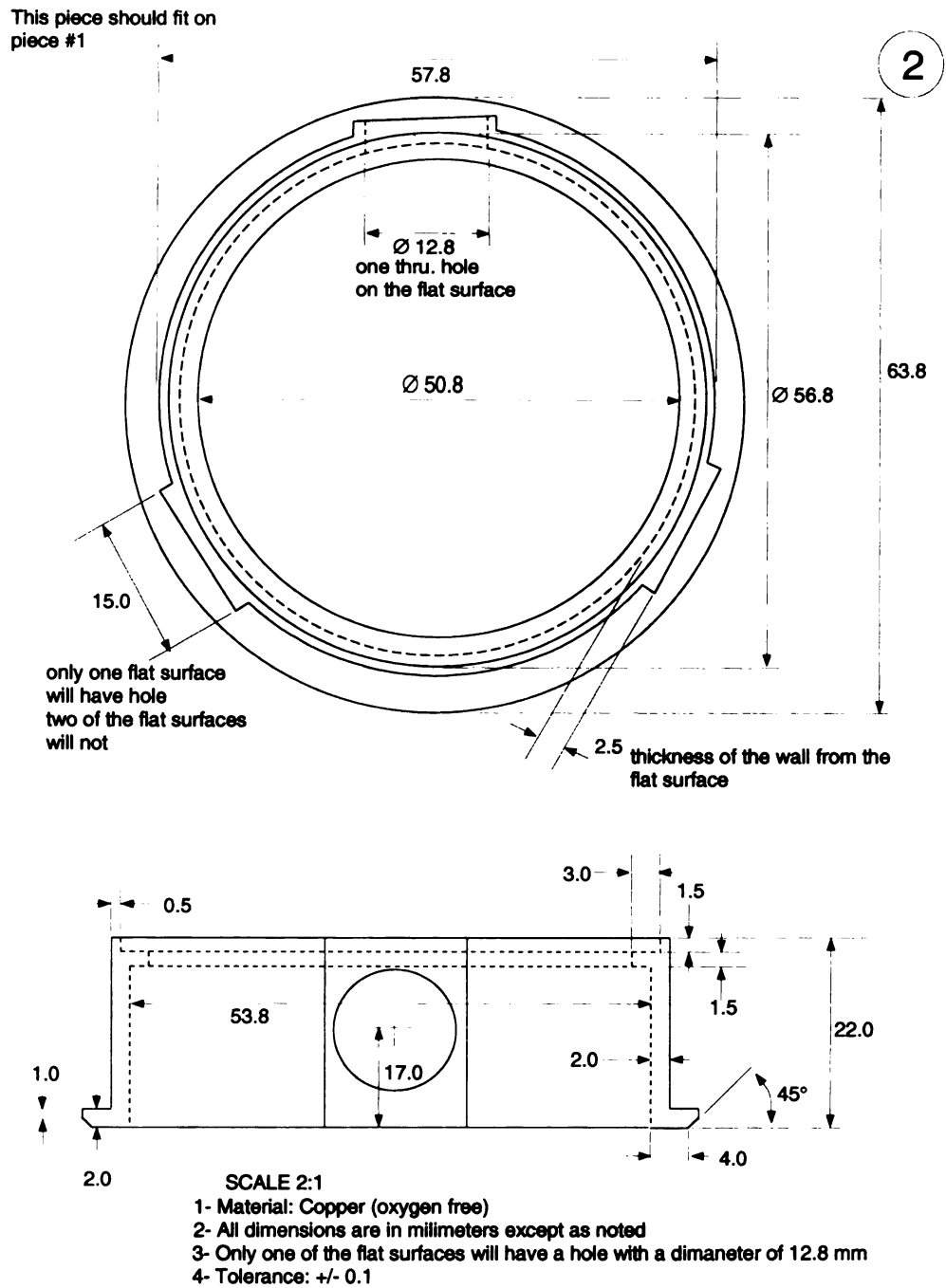
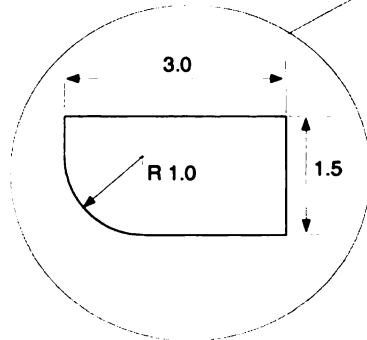
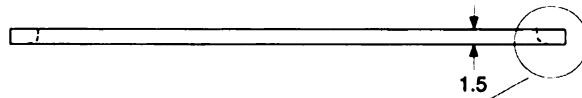
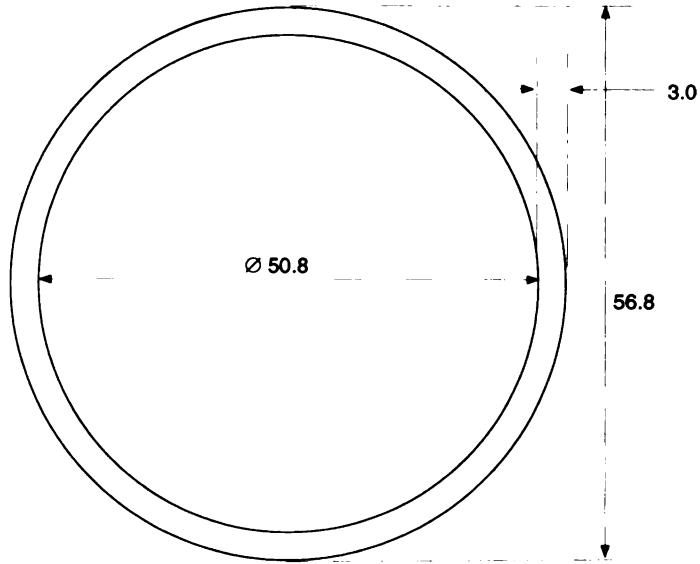


Figure A.3: The cover of the chamber. The window material is thin *Kapton*[®] polyimide film for minimum X-ray absorption. Feedthrough is also made in-house.

This piece should fit on piece #2

3

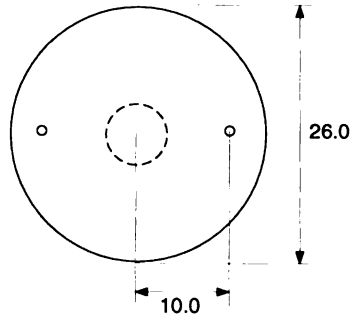


SCALE 2:1

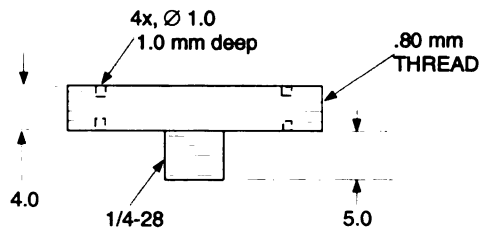
- 1- Material: Stainless Steel
- 2- All dimensions are in millimeters
- 3- Tolerance: +/- 0.1

Figure A.4: Stainless steel ring to lock the window.

4



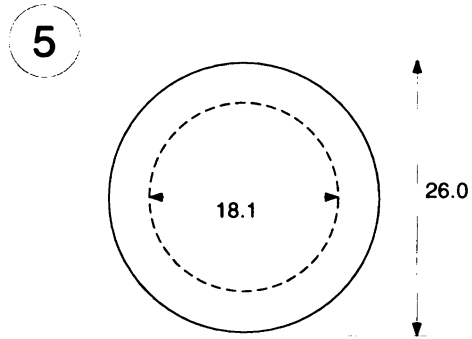
This piece should fit
in piece #1
Flat surfaces should touch
each other for thermal conductivity



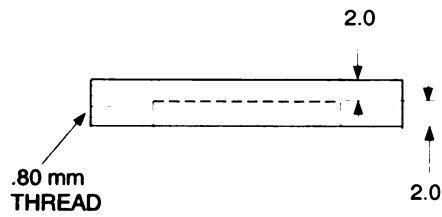
SCALE 2:1

- 1- Material: Copper (oxygen free)
- 2- All dimensions are in millimeters
- 3- Tolerance: +/- 0.1

Figure A.5: Apparatus to use the heat exchange chamber in closed cycle displax refrigerators.



This piece should fit
in piece #1
Flat surfaces should touch
each other for thermal conductivity



SCALE 2:1

- 1- Material: Copper (oxygen free)
- 2- All dimensions are in millimeters
- 3- Tolerance: +/- 0.1

Figure A.6: Apparatus to use the heat exchange chamber in a flow cryostat.

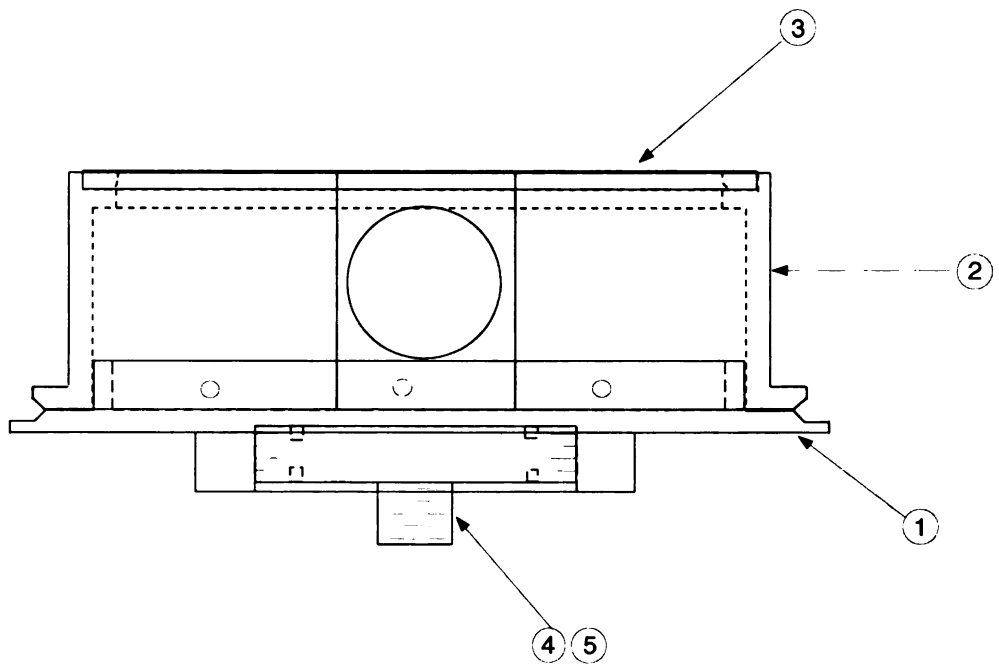


Figure A.7: Air is sealed in the chamber to guarantee temperature uniformity.

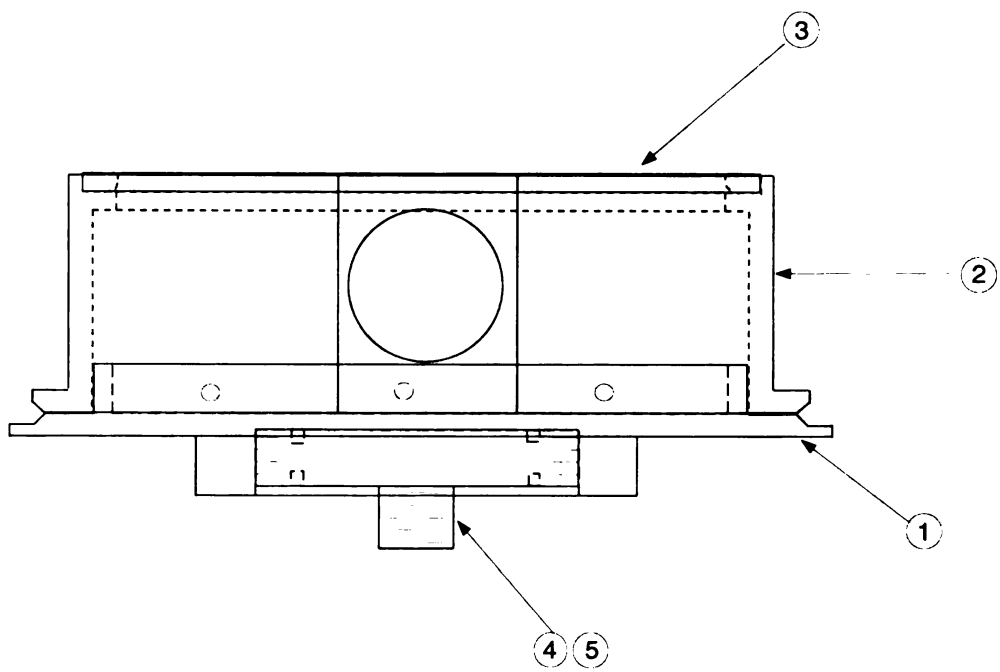


Figure A.7: Air is sealed in the chamber to guarantee temperature uniformity.

Bibliography

- [1] D. T. Bowron, M. H. Krisch, A. C. Barnes, J. L. Finney, A. Kaprolat, and M. Lorenzen. X-ray-raman scattering from the oxygen k edge in liquid and solid h_2o . *Phys. Rev. B*, 62(14):R9223–R9227, Oct 2000.
- [2] Jens Als-Nielsen and Des McMorrow. *Elements of Modern X-ray Physics*. John Wiley & Sons, Ltd., 2001.
- [3] J. van den Brink and M. van Veenendaal. Correlation functions measured by indirect resonant inelastic x-ray scattering. *EPL (Europhysics Letters)*, 73(1):121–127, 2006.
- [4] P. Becker, P. Scyfried, and H. Siegert. The lattice parameter of highly pure silicon single crystals. *Zeitschrift für Physik B Condensed Matter*, 48:17–21, 1982.
- [5] M. Y. Hu, H. Sinn, A. Alatas, W. Sturhahn, E. E. Alp, H. C. Wille, Yu. V. Shvyd’ko, J. P. Sutter, J. Bandaru, E. E. Haller, V. I. Ozhogin, S. Rodriguez, R. Colella, E. Kartheuser, and M. A. Villeret. Effect of isotopic composition on the lattice parameter of germanium measured by x-ray backscattering. *Phys. Rev. B*, 67(11):113306, Mar 2003.
- [6] R.E. Newnham and Y.M. De Haan. Refinement of the α - al_2o_3 , ti_2o_3 , v_2o_3 , and cr_2o_3 structures. *Zeitschrift für Kristallographie*, 117:235, 1962.
- [7] A. Alatas. PhD thesis, Illinois Institute of Technology, 2002.
- [8] R. Stedman, Z. Amilius, R. Pauli, and O. Sundin. Phonon spectrum of beryllium at 80k. *J. Phys. F: Metal Phys.*, 6(2):157–166, 1976.
- [9] W. C. Röntgen. Weitere beobachtungen ber die eigenschaften der x-strahlen. *Annalen der Physik*, 300(1):18–37, 1898.
- [10] Charles G Barkla. Energy of secondary röntgen radiation. *Proceedings of the Physical Society of London*, 19(1):185–204, 1903.
- [11] H. G. J. Moseley. The high frequency spectra of the elements. *Philosophical Magazine*, 26:1024–1034, 1913.
- [12] W. Friedrich, P. Knipping, and M. von Laue. *Sber. Math. Phys. Kl. K. Bayer. Akad. Wiss. München*, pages 303–322, 1912.

- [13] W. L. Bragg. *Proc. Cambridge Phil. Soc.*, 17:43, 1913.
- [14] W. H. Bragg and W. L. Bragg. *Proc. Royal Soc., A* 88:428438, 1913.
- [15] P. Debye. Interferenz von rntgenstrahlen und wrmebewegung. *Annalen der Physik*, 348(1):49–92, 1913.
- [16] Arthur H. Compton. A quantum theory of the scattering of x-rays by light elements. *Phys. Rev.*, 21(5):483–502, May 1923.
- [17] I. Waller. *Z. Physik*, 17:398, 1923.
- [18] P. Olmer. Dispersion des vitesses des ondes acoustiques dans l'aluminium. *Acta Crystallographica*, 1(2):57–63, May 1948.
- [19] Robert Weinstock. Inelastic scattering of slow neutrons. *Phys. Rev.*, 65(1-2):1–20, Jan 1944.
- [20] B. N. Brockhouse and D. G. Hurst. Energy distribution of slow neutrons scattered from solids. *Phys. Rev.*, 88(3):542–547, Nov 1952.
- [21] B. N. Brockhouse and P. K. Iyengar. Normal modes of germanium by neutron spectrometry. *Phys. Rev.*, 111(3):747–754, Aug 1958.
- [22] B. Dorner, E. Burkel, and J. Peisl. An x-ray backscattering instrument with very high energy resolution. *Nuclear Instruments and Methods in Physics Research Section A*, 246:450–451, 1986.
- [23] E. Burkel, J. Peisl, and B. Dorner. Observation of inelastic X-ray scattering from phonons. *Europhysics Letters*, 3:957–+, April 1987.
- [24] B. Dorner, E. Burkel, Th. Illini, and J. Peisl. First measurement of a phonon dispersion curve by inelastic x-ray scattering. *Zeitschrift fr Physik B*, 69(2-3):179–183, 1987.
- [25] Harald Sinn. Spectroscopy with mev energy resolution. *Journal of Physics: Condensed Matter*, 13(34):7525–7537, 2001.
- [26] Cullie J. Sparks. Inelastic resonance emission of x rays: Anomalous scattering associated with anomalous dispersion. *Phys. Rev. Lett.*, 33(5):262–265, Jul 1974.
- [27] J. P. Hill, C.-C. Kao, W. A. L. Caliebe, M. Matsubara, A. Kotani, J. L. Peng, and R. L. Greene. Resonant inelastic x-ray scattering in nd_2cuo_4 . *Phys. Rev. Lett.*, 80(22):4967–4970, Jun 1998.
- [28] P. Abbamonte, C. A. Burns, E. D. Isaacs, P. M. Platzman, L. L. Miller, S. W. Cheong, and M. V. Klein. Resonant inelastic x-ray scattering from valence excitations in insulating copper oxides. *Phys. Rev. Lett.*, 83(4):860–863, Jul 1999.

- [29] M. Z. Hasan, E. D. Isaacs, Z.-X. Shen, L. L. Miller, K. Tsutsui, T. Tohyama, and S. Maekawa. Electronic Structure of Mott Insulators Studied by Inelastic X-ray Scattering. *Science*, 288(5472):1811–1814, 2000.
- [30] J. G. Bednorz and K. A. Müller. Possible high-temperature superconductivity in the barium system. *Zeitschrift für Physik B Condensed Matter*, 64:189–193, 1986.
- [31] E. Burkel. *Inelastic Scattering of X-rays with Very High Energy Resolution*, volume 125. Springer, Berlin, 1991.
- [32] H. A. Kramers and W. Heisenberg. *Zeitschrift für Physik*, 31:681–708, 1925.
- [33] K. Okada and A. Kotani. Copper k and oxygen k resonant inelastic x-ray scattering of one-dimensional cuprates. *Journal of the Physical Society of Japan*, 75(4):044702, 2006.
- [34] S. M. Butorin. Resonant inelastic x-ray scattering as a probe of optical scale excitations in strongly electron-correlated systems: quasi-localized view. *Journal of Electron Spectroscopy and Related Phenomena*, 110-111:213–233, 2000.
- [35] Akio Kotani and Shik Shin. Resonant inelastic x-ray scattering spectra for electrons in solids. *Rev. Mod. Phys.*, 73(1):203–246, Feb 2001.
- [36] B. S. Asbrink and L. J. Norrby. *Acta. Crystallogr.*, B26:8–15, 1970.
- [37] D. Souptel, G. Behr, and A.M. Balbashov. Srzro3 single crystal growth by floating zone technique with radiation heating. *Journal of Crystal Growth*, 236:583–588(6), 2002.
- [38] William H. Zachariasen. *Theory of X-ray Diffraction in Crystals*. Dover Publications, 1994.
- [39] Andre Authier. *Dynamical Theory of X-Ray Diffraction*. Oxford University Press, 2001.
- [40] Yu.V. Shvyd'ko. *X-Ray Optics: High-Energy-Resolution Applications*, volume 98. Springer, 2004.
- [41] Yu.V. Shvyd'ko and E. Gerdau. Backscattering mirrors for x-rays and mssbauer radiation. *Hyperfine Interactions*, 123-124(1):741–776, 1999.
- [42] R.W. James. The dynamical theory of x-ray diffraction. *Solid State Physics*, 15:53–220, 1963.
- [43] Jesse W. M. DuMond and Harry A. Kirkpatrick. The multiple crystal x-ray spectograph. *Rev. Sci. Inst.*, 1(2):88–105, 1930.
- [44] Max Born and Emil Wolf. *Principles of Optics*. Cambridge University Press, 1999.

- [45] C. Masciovecchio, U. Bergmann, et al. A perfect crystal x-ray analyser with mev energy resolution. *Nucl. Instrum. Methods B*, 111:181–186, Apr 1996.
- [46] S. Takagi. Dynamical theory of diffraction applicable to crystals with any kind of small distortion. *Acta Cryst.*, 15(12):1311–1312, Dec 1962.
- [47] D. Taupin. *Bull. Soc. Fr. Min. Crist.*, 87:469–511, 1964.
- [48] P. Suortti et al. On the phase-space description of synchrotron x-ray beams. *Rev. Sci. Inst.*, 60:2579–2585, 1989.
- [49] Th. Illini. Master’s thesis, Ludwig Maximillians Universität München, 1986.
- [50] H. Yavaş, E. E. Alp, H. Sinn, et al. A high-resolution rixs spectrometer for correlated electron materials. *AIP Conference Proc.*, 789:299–305, 2005.
- [51] D. Tabor. Mohs’s hardness scale—a physical interpretation. *Proceedings of the Physical Society B*, 67:249, 1954.
- [52] C. G. Peters and F. Knoop. Metals in thin layers—their microhardness. *Metals and Alloys*, 13:292, 1940.
- [53] A. Reisman, M. Berkenblit, J. Cuomo, and S. A. Chan. The chemical polishing of sapphire and mgal spinel. *Journal of The Electrochemical Society*, 118(10):1653–1657, 1971.
- [54] A. Roth. *Vacuum Sealing Techniques*. Springer, New York, 1994.
- [55] C. Liu, R. Conley, and A. T. Macrander. Functional profile coatings and film stress. *J. Vac. Sci. Technol. A*, 22:1610–1614, 2004.
- [56] E. D. Case and M. A. Crimp. Joining of ceramic materials using spin-on interlayers. *Advanced Engineering Materials*, 3(6):395–399, 2001.
- [57] G. K. White and R. B. Roberts. Thermal expansion of reference materials: tungsten and $\alpha\text{-Al}_2\text{O}_3$. *High Temperatures - High Pressures*, 15:321–328, 1983.
- [58] R. J. McQueeney, Y. Petrov, T. Egami, M. Yethiraj, G. Shirane, and Y. Endoh. Anomalous dispersion of lo phonons in $\text{La}_{1.85}\text{Sr}_{0.15}\text{CuO}_4$ at low temperatures. *Phys. Rev. Lett.*, 82(3):628–631, Jan 1999.
- [59] T. Egami. Electron-lattice interaction in cuprates. *Journal of Low Temperature Physics*, 105:791–800, 1996.
- [60] D. Reznik, L. Pintschovius, M. Ito, S. Iikubo, M. Sato, H. Goka, M. Fujita, K. Yamada, G. D. Gu, and J. M. Tranquada. Electron-phonon coupling reflecting dynamic charge inhomogeneity in copper oxide superconductors. *Nature*, 440:1170–1173, 2006.

- [61] F. P. Koffyberg and F. A. Benko. A photoelectrochemical determination of the position of the conduction and valence band edges of p-type cuo. *Journal of Applied Physics*, 53(2):1173–1177, 1982.
- [62] J. C. Irwin, J. Chrzanowski, T. Wei, D. J. Lockwood, and A. Wold. Raman scattering from single crystals of cupric oxide. *Physica C: Superconductivity*, 166:456–464, 1990.
- [63] H. F. Goldstein, Dai-sik Kim, Peter Y. Yu, L. C. Bourne, J-P. Chaminade, and Leon Nganga. Raman study of cuo single crystals. *Phys. Rev. B*, 41(10):7192–7194, Apr 1990.
- [64] G. Kliche and Z. V. Popovic. Far-infrared spectroscopic investigations on cuo. *Phys. Rev. B*, 42(16):10060–10066, Dec 1990.
- [65] W. Reichardt, F. Gompf, M. An, and B. M. Wanklyn. Lattice dynamics of cupric oxide. *Zeitschrift fr Physik B*, 81:19–24, 1990.
- [66] Hasan Yavas, E. Ercan Alp, Harald Sinn, Ahmet Alatas, Ayman H. Said, Yuri Shvyd'ko, Thomas Toellner, Ruben Khachatryan, Simon J.L. Billinge, M. Zahid Hasan, and Wolfgang Sturhahn. Sapphire analyzers for high-resolution x-ray spectroscopy. *Nuclear Instruments and Methods in Physics Research Section A*, 582:149–151, 2007.
- [67] Stephen W. Lovesey. *Theory of Neutron Scattering from Condensed Matter*. Oxford University Press, 1984.

MICHIGAN STATE UNIVERSITY LIBRARIES



3 1293 02956 3248